nature structural & molecular biology

Article

https://doi.org/10.1038/s41594-026-01893-6

Ligand-dependent G protein dynamics underlying opioid efficacy

Received: 18 May 2025

Accepted: 26 August 2026

Published online: 13 October 2026

Check for updates

Jonathan C. Deutsch[1,2], Daniel Hilger[3], John Janetzko[2,6], Charles M. Schroeder[1,4,7], Steven Chu[2,5], Brian K. Kobilka[2] ✉ & Rabindra V. Shivnaraine[2,8] ✉

Activation of heterotrimeric G proteins by G-protein-coupled receptors (GPCRs) requires large-scale opening of the Gα α-helical domain (AHD) to expose the nucleotide-binding site and facilitate GDP–GTP exchange. Although orthosteric ligands are known to modulate GPCR conformation, how these effects propagate to the bound G protein remains unclear. Using single-molecule Förster resonance energy transfer imaging, we monitored AHD motions in G_i proteins coupled to the μ-opioid receptor across different ligand- and nucleotide-bound states. We find that receptor ligands differentially modulate these dynamics from a binding site over 70 Å away, with higher-efficacy agonists accelerating transitions to an open, low-nucleotide-affinity conformation. These data also capture transient AHD intermediates during nucleotide exchange and suggest that allosteric control over the G protein conformational states provides an additional mechanism for encoding opioid efficacy and signaling outcomes.

Full and partial agonists have distinct therapeutic applications for targeting opioid receptors, with full agonists used in pain management and partial agonists in treatment of opioid use disorder. The μ-opioid receptors (μORs) are G-protein-coupled receptors (GPCRs) that mediate analgesia and reward responses to common opioid drugs by catalyzing guanine nucleotide exchange in heterotrimeric G_i proteins, composed of Gα, Gβ and Gγ subunits[1]. When activated by ligands, μOR and other class A GPCRs couple to inactive, GDP-bound G proteins at their intracellular surface (Fig. 1a). This interaction induces conformational changes in the G protein that promote GDP release and GTP binding, activating the G protein and triggering downstream signaling cascades that effectuate the physiological response[2]. Recent biophysical evidence indicates that ligands modulate GPCR signaling by stabilizing distinct receptor conformational states that vary in their G-protein-coupling efficiency[3–9]. However, the extent to which these ligand-dependent states propagate to the coupled G protein remains unclear and, if they do, whether these altered G protein conformational states also affect signaling outcomes in the cell.

The most notable conformational change observed for G protein activation by a GPCR is the separation of its Ras-like and α-helical domains (RLD and AHD) in the Gα subunit (Fig. 1a,b), as revealed by early double electron–electron resonance (DEER) spectroscopy[10] and X-ray crystallography[11] studies. In all inactive-state crystal structures, the AHD—a six-α-helical bundle (αA–αF)—packs against the RLD, burying the bound GDP in the interface between the domains[12]. Following receptor coupling and GDP release, this interface opens by tens of angstroms[10,11,13–15], resulting in an intrinsically dynamic AHD that has largely eluded high-resolution structural characterization[16].

Multiple lines of evidence suggest that AHD movements are critical for facilitating GDP–GTP exchange across all G protein isoforms,

[1]Center for Biophysics and Quantitative Biology, University of Illinois Urbana-Champaign, Urbana, IL, USA. [2]Department of Molecular and Cellular Physiology, Stanford University, Stanford, CA, USA. [3]Department of Pharmaceutical Chemistry, Philipps-University Marburg, Marburg, Germany. [4]Departments of Materials Science and Engineering, Chemical and Biomolecular Engineering, and Chemistry, University of Illinois Urbana-Champaign, Urbana, IL, USA. [5]Departments of Physics, Energy Sciences, and Engineering, Stanford University, Stanford, CA, USA. [6]Present address: Department of Biochemistry and Molecular Genetics, University of Colorado Anschutz Medical Campus, Aurora, CO, USA. [7]Present address: Department of Chemical and Biological Engineering, Princeton University, Princeton, NJ, USA. [8]Present address: Aerys Biosciences, Palo Alto, CA, USA. ✉e-mail: kobilka@stanford.edu; rvshiv@stanford.edu

https://doi.org/10.1038/s41594-026-01893-6

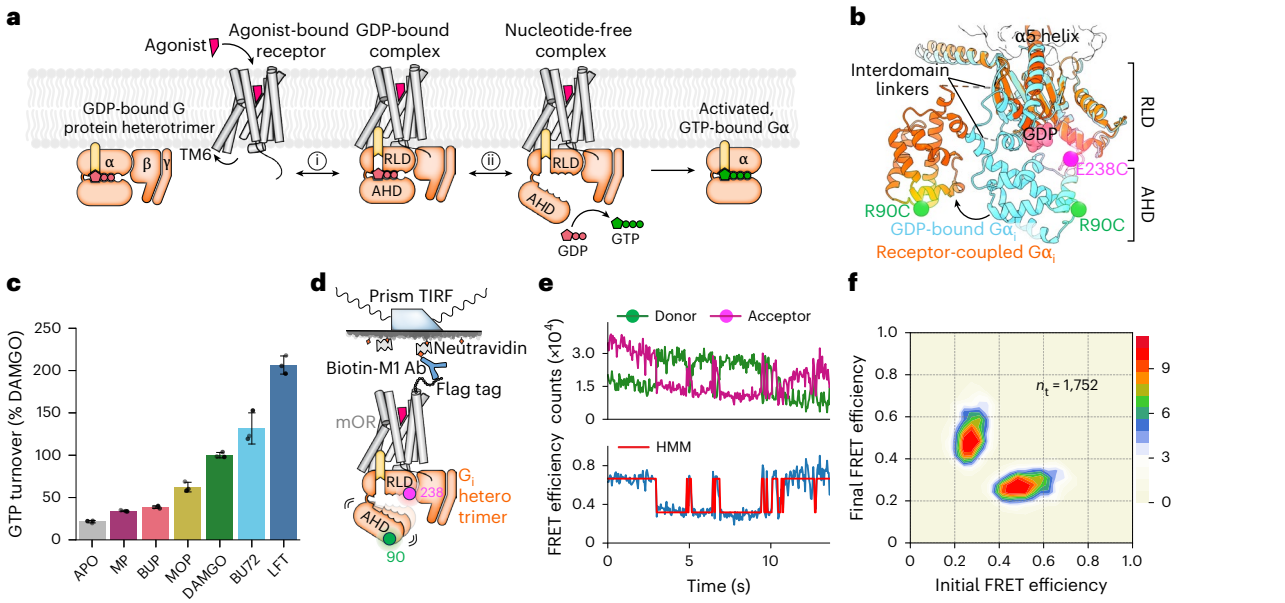


Fig. 1 | G protein conformational dynamics facilitate μOR–G_i activation. **a**, Agonist binding to a class A GPCR promotes G protein coupling and activation through GDP–GTP exchange. The activation rate can be influenced by the rate of initial receptor–G protein coupling (i) or through modulating the G protein conformational changes that facilitate nucleotide exchange (ii). **b**, Labeling sites R90C (green) and E238C (magenta) shown on superimposed $G\alpha_i$ structures in the inactive (GDP-bound) state (PDB 1GP2) and in the receptor-coupled (nucleotide-free) state with an open AHD (PDB 7L0Q). **c**, Ligand efficacy profiles determined from $G\alpha_i\Delta$6-90C/238C GTP turnover assay (Methods). Error bars denote the mean ± s.d. from three technical replicates. **d**, Schematic of smFRET experiments. **e**, Example single-molecule fluorescence (top) and apparent FRET efficiency (bottom) time traces of surface-tethered μOR–G_i bound to full agonist LFT, displaying transitions between a low-FRET, open state and a high-FRET, closed state. **f**, Transition density plot displaying the mean FRET values before (*x* axis) and after (*y* axis) each transition for LFT–μOR–G_i (scale bar, 10^{-3} transitions per bin per second; n_t total transitions).

yet their role in signaling efficacy remains poorly understood[17]. While molecular dynamics (MD) simulations indicate that domain separation alone may not be sufficient for nucleotide exchange, a variety of functional[18–20], spectroscopic[13,21,22] and computational[23,24] studies demonstrate that AHD movements are tightly linked to both GDP release and the subsequent binding of GTP[16,25,26]. Here, we use total internal reflection fluorescence (TIRF) single-molecule Förster resonance energy transfer (smFRET) imaging to directly monitor AHD motions in G_{i1} proteins bound to μOR activated by diverse orthosteric ligands, in the absence and presence of nucleotide. Our results reveal how ligand-specific signals are allosterically encoded in the G protein conformational ensemble, a pattern that also applied to G_i bound to neurotensin type 1 receptor (NTSR1). These data suggest a mechanistic basis for opioid signaling efficacy that extends beyond simple receptor–G protein coupling efficiency.

Results

Donor and acceptor fluorophores (LD555 (ref. 27) and JFX673 (ref. 28), respectively) were labeled on the AHD (R90C) and RLD (E238C) of a previously reported minimal cysteine $G\alpha_{i1}$ mutant[10,29] (Fig. 1b, Extended Data Fig. 1a and Methods). This construct, $G\alpha_i\Delta$6-90C/238C, exhibited a wild type (WT)-like rank order of ligand -dependent GTP turnover with μOR in vitro (Fig. 1c and Extended Data Fig. 1b) and, consistent with earlier characterizations, its activity was not impaired compared to the WT protein (Extended Data Fig. 1c). LD555/JFX673-labeled $G\alpha_i\Delta$6-90C/238C heterotrimers efficiently coupled to agonist-bound μOR, forming stable, nucleotide-depleted ternary complexes (Extended Data Fig. 1d). For TIRF imaging (Methods), these μOR–G_i ternary complexes were specifically immobilized on quartz slides with an M1 Fab fragment (Fig. 1d and Extended Data Fig. 1e), remaining functional when tethered to the surface as confirmed by GTPγS-induced G protein dissociation (Extended Data Fig. 1f). Time-dependent changes in AHD position were captured from smFRET trajectories of individual, immobilized μOR–G_i complexes, which displayed reversible transitions (on the order of 1 s^{-1}) between low-FRET and high-FRET states (Fig. 1e,f). These dynamics reflect spontaneous domain separation and reengagement consistent with the various poses observed in previous negative-stain and cryo-electron microscopy (cryo-EM) studies of a receptor–G protein complex[16,26].

Ligand-induced AHD opening

We examined the impacts of μOR bound to ligands with varying signaling efficacies (Fig. 1c), as well as the unliganded (apo) receptor, on AHD dynamics in coupled G_i heterotrimers (Fig. 2a and Extended Data Fig. 2a). These ligands included strong full agonists lofentanil (LFT) and BU72 (ref. 30), the endogenous enkephalin-like full agonist DAMGO, the partial agonist morphine (MOP) and weaker partial agonists buprenorphine (BUP) and mitragynine pseudoindoxyl. Apparent population FRET efficiencies for all ligands showed two predominant states, centered at ~0.27 and ~0.62, along with a minor ~0.47 FRET population that remained constant across all samples. At μOR bound to full agonists, occupancy of the low-FRET (0.27) state increased relative to partial agonists, whereas that of the high-FRET (0.62) state decreased (Fig. 2a). This ligand-induced low-FRET occupancy was strongly correlated with in vitro GTP turnover activity (a direct measure of efficacy) (R^2 = 0.97; Fig. 2b), indicative of an open Gα conformation like that seen in active-state complex structures[11,14] (Fig. 1b). Likewise, apo μOR was the least efficient at stabilizing this low-FRET, open conformation, in line with its slow GTP turnover under basal conditions (Fig. 2a,b). In addition, the apo complex exhibited a small population (~10%) from excursions to >0.7 FRET (fit as a fourth Gaussian state), which the AHD rarely sampled under liganded conditions (Fig. 2a and Extended Data Fig. 2a).

To investigate the kinetics of AHD motions within μOR–G_i, we used a hidden Markov model (HMM) to idealize the traces and quantify transitions between high-FRET and low-FRET states (Figs. 1e and 2c and Methods). The occupancy of the mid-FRET (~0.47) state was not

https://doi.org/10.1038/s41594-026-01893-6

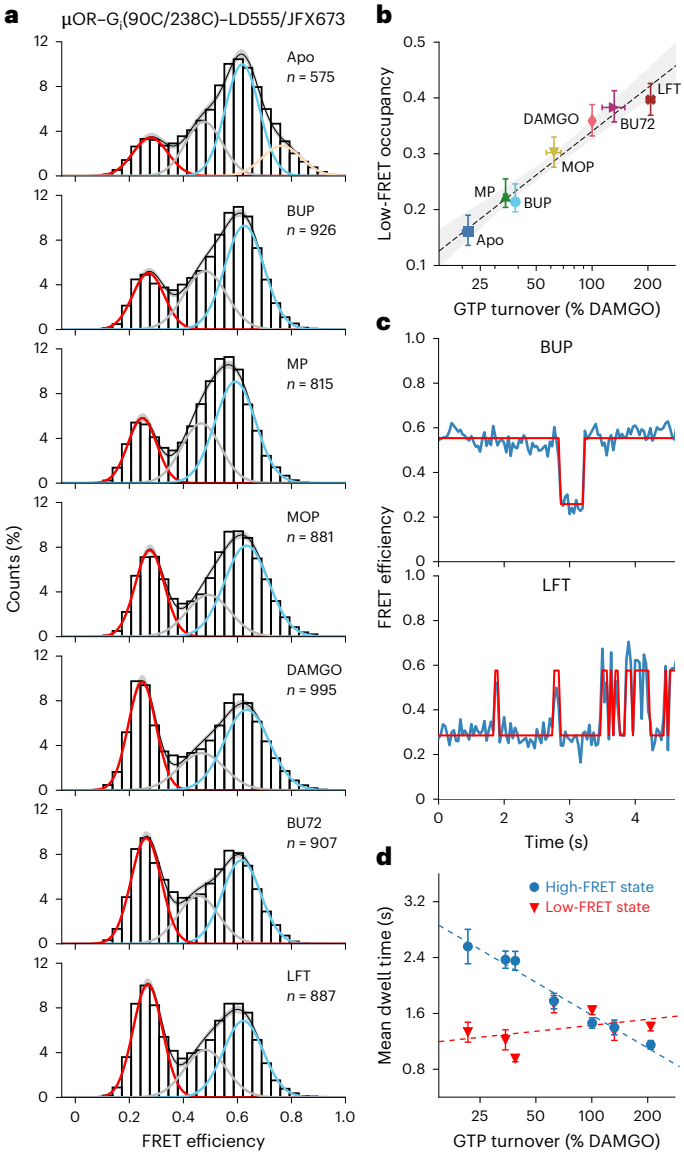


Fig. 2 | AHD opening is ligand efficacy dependent. a, Apparent population FRET efficiency histograms for μOR–G_i ternary complexes fit to three-state or four-state GMM (black curves), showing the open (red) and closed (cyan) substates (*n*, number of traces). Shaded error bands represent ±1 s.d. of GMM fits from 1,000 bootstrap samples of the FRET traces. **b**, Scatter plot of ensemble average low-FRET, open-state occupancies obtained from the GMM fits (error bars, bootstrapped 95% CI) and mean GTP turnover activities (error bars, s.d. of $n = 3$) observed for each ligand with log-linear regression (dashed line; $R^2 = 0.97$; error band, 95% CI of the fit). **c**, Example FRET (blue) and predicted state (red) traces for partial (top; BUP) and full (bottom; LFT) agonists. **d**, Mean dwell times in the low-FRET, open and high-FRET, closed states for each ligand. Data represent the mean ± s.d. of 100 bootstrap samples of the idealized traces, plotted against GTP turnover with log-linear fits (as in **b**).

ligand dependent (Fig. 2a) and was sampled transiently, with nearly half of its occurrences lasting two frames or less (≤100 ms). Hence, the mid-FRET state may reflect an unstable conformational intermediate and/or result from time-averaging of rapid (>10 s^{-1}) low-FRET to high-FRET excursions at the current imaging speed. Because neither mid-FRET transitions nor distributions could be cleanly distinguished from the high-FRET state at the aggregate level (Extended Data Fig. 2b and Fig. 2a), we analyzed the kinetics as a two-state system, where the mid-FRET and the high-FRET states are collapsed into a single, broadly distributed (~0.4–0.6) closed conformation.

This analysis revealed that increasing ligand efficacy at μOR enhances the overall level of dynamics within coupled G_i heterotrimers (Fig. 2c and Extended Data Fig. 2b,c), primarily by reducing the duration that the AHD dwelled in the closed, high-FRET state (Extended Data Fig. 2c). Mean dwell times in this high-FRET state (τ_{high}) depended strongly on ligand efficacy ($R^2 = 0.97$; Fig. 2d), with the apparent rate of AHD opening being approximately 2.25-fold faster for LFT-occupied compared to apo-occupied complexes (~0.9 s^{-1} and ~0.4 s^{-1}, respectively). Conversely, dwell times in the low-FRET state were similar (~1.4 s on average) across all ligands tested ($R^2 = 0.15$; Fig. 2d and Extended Data Fig. 2c). Thus, ligand-dependent shifts in the AHD's conformational equilibrium (Fig. 2a) stem from the destabilization of its closed state, rather than stabilization of the open, domain-separated conformation. This indicates that efficacy is, at least in part, dependent on the ability of the ligand to allosterically initiate domain separation rather than merely to promote receptor conformations that affect initial G protein coupling.

While domain separation is key for receptor-catalyzed GDP release, the observed high-FRET to low-FRET transition rates are slower (approximately tenfold) than timescales expected from receptor–G protein association measurements in living cells (<100–300 ms)[31,32]. However, cellular G protein activation rates inferred from Gα and βγ subunit separation (~0.5–2 s)[33–35] more closely match the smFRET dynamics observed here, consistent with AHD opening and GDP release occurring after initial formation of the receptor-transducer complex. The absolute values of these rates may nevertheless be influenced by experimental conditions, such as the detergent micelle, cysteine substitutions, temperature and/or limitations in imaging speed and fluorescent probes. In addition, we note the high-FRET dwell time distributions appear heterogeneous (Extended Data Fig. 2c), with a fast component for full agonists that overlaps the reported cellular coupling timescales.

Parallel smFRET imaging of NTSR1–G_i ternary complexes (Methods), which couple promiscuously in vitro, yielded a correlation between agonist-induced low-FRET occupancy and GTP turnover similar to that of μOR ($R^2 = 0.89$; Extended Data Figs. 3 and 4 and Fig. 2b). The addition of SBI-553, an allosteric modulator shown to elicit an effector-dependent response[36], further shifted the AHD toward the open state proportionally to its positive modulation of GTP turnover in vitro (Extended Data Fig. 3b). These findings suggest that AHD displacement may be a general determinant of ligand efficacy across G protein–receptor pairs, consistent with previous bioluminescence resonance energy transfer (BRET) studies showing distinct G protein conformational signatures for different calcitonin and α2-adrenergic receptor ligands[22,37].

AHD conformations in the basal state

In basal (inactive)-state structures of heterotrimeric G proteins, the Gα AHD tightly encloses the bound GDP[38,39], yet spontaneous domain separation must occur to permit GDP release, as G proteins still slowly exchange nucleotide even without GPCR catalysis[40]. To investigate these basal dynamics, we immobilized labeled G_i heterotrimers using an N-terminal histidine tag and imaged their AHD motions in a physiological concentration of GDP (30 μM)[41] (Extended Data Fig. 5a and Methods).

Compared to receptor-bound G protein, basal G_i showed greater conformational heterogeneity (≥3–4 distinct states) and reduced average interdomain separation, primarily because of the AHD populating an additional (inactive, high-FRET) state centered at ~0.77 (Extended Data Fig. 5b–d). This inactive state corresponds to an interdye distance consistent with full domain closure (Δopen–closed ≈ 28 Å) and likely resembles the GDP-bound conformation seen in the inactive-state G_i crystal structure[38] (Fig. 1b). These data predict that even in its 'closed' (0.62) high-FRET state, the receptor-coupled G_i AHD remains partially displaced (~5–8 Å). Elimination of the fully

https://doi.org/10.1038/s41594-026-01893-6

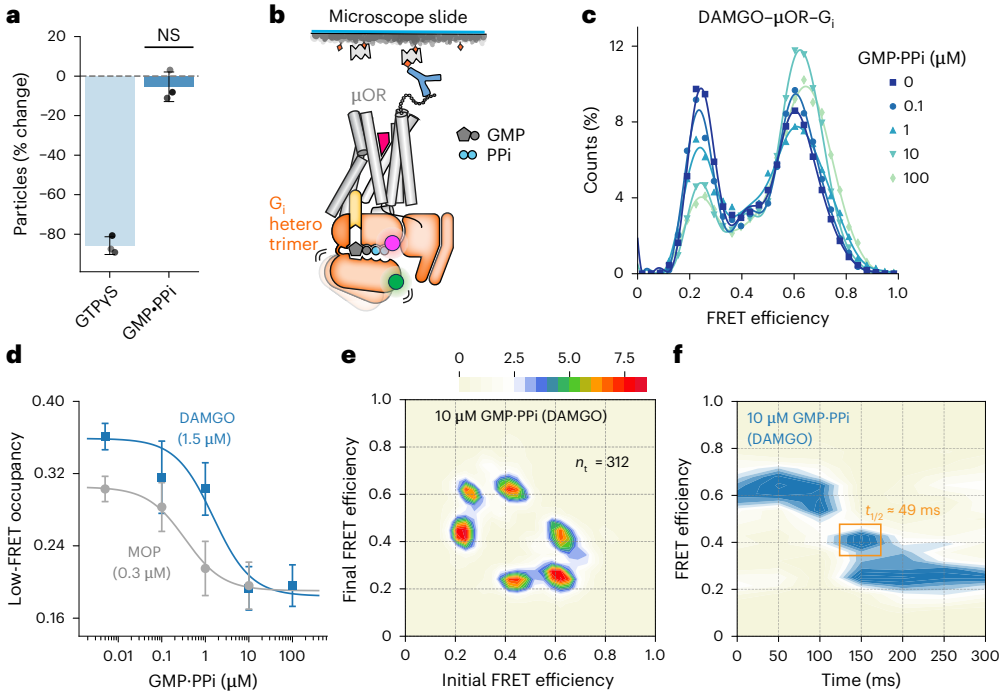


Fig. 3 | Nucleotide binding promotes AHD closure through an intermediate. **a**, GTPγS, but not GMP added together with PPi, dissociates G protein from surface-tethered μOR. Error bars denote the mean ± s.d. ($n = 3$ videos from the same sample) of the percentage change in FRET particles remaining after delivery of 10 μM nucleotide; $P = 0.4$ (not significant, NS) according to a two-sided, unpaired Welch's t-test on the unnormalized counts. **b**, Schematic of single-molecule GMP·PPi titration experiments. **c**, Population FRET efficiency histograms (symbols) with B-spline fits (lines) for DAMGO-bound μOR–G_i in the presence of increasing concentrations of GMP·PPi. **d**, Apparent EC_{50} values measured from GMP·PPi-induced ensemble average low-FRET occupancy for DAMGO (blue) and MOP (gray); error bars denote the s.d. of 1,000 bootstrap samples of the FRET traces (3,323 molecules total across all conditions). Lines are the s.d.-weighted fits to three-parameter dose–response functions (Hill slope = 1). **e**,**f**, Transition density plot (**e**) for DAMGO with 10 μM GMP·PPi (scale bar, 10^{-3} transitions per bin per second; n_t total transitions) and contour plot of synchronized high-to-low transitions (**f**) showing a short-lived dwell in a mid-FRET state (yellow box, width ≈ one frame; 100 transition events) (Extended Data Fig. 6e). Synced data are unidealized FRET.

closed (0.77 FRET) conformation upon agonist-stimulated receptor–G protein complex assembly (Fig. 2a and Extended Data Fig. 3a) is, therefore, consistent with destabilization of the AHD–RLD interactions that most tightly enclose GDP.

Under basal conditions, individual G_i AHDs exhibited fewer transitions at this temporal resolution but still sampled the open state at low frequency (Extended Data Fig. 5c,d), as seen in prior MD simulations[23]. These transitions predominantly traveled through an apparent mid-FRET (~0.4–0.5) intermediate state (Extended Data Fig. 5d), suggesting that a partially open AHD could mediate transitions between the GDP-bound and fully open conformations. Introducing an alanine substitution at residue R144 in the α subunit (Extended Data Fig. 5e), previously shown to destabilize the RLD–AHD interaction and enhance basal nucleotide exchange[40,42], depleted the very-high-FRET, GDP-bound conformation and shifted the AHD toward more open states while preserving some transition paths similar to those observed for the receptor-bound G protein (Extended Data Fig. 5f–h). G_i immobilized without receptor and depleted of GDP (Methods) yielded a broad distribution centered around this same mid-FRET range (Extended Data Fig. 5i), further supporting assignment of this intermediate as a lower-GDP-affinity conformation that dominates the nucleotide-free ensemble in the absence of receptor engagement.

Nucleotide effects on intact μOR–G_i complexes

As described above, the AHD can adopt at least four distinct FRET states: (1) a low-FRET, open state (~0.27) that correlates with ligand efficacy; (2) a short-lived, intermediate state (~0.47); (3) a high-FRET, closed state (~0.62) while the G protein is receptor bound; and (4) an inactive, GDP-bound closed state (~0.77) seen basally in uncoupled G_i. The FRET states observed in receptor-coupled G proteins (0.27, 0.47 and 0.62) could not be directly linked to stable nucleotide binding, as GTP or GDP delivery caused rapid dissociation from the receptor, precluding equilibrium observation of bound states (Fig. 3a). However, GMP and pyrophosphate (PPi) (Extended Data Fig. 6a), which together mimic GTP binding in the nucleotide pocket of small G proteins[43], did not significantly dissociate the complex (Fig. 3a,b).

Using this approach with surface-tethered μOR–G_i complexes activated by DAMGO (Fig. 3c–f and Extended Data Fig. 6b–e), we observed a concentration-dependent shift from open to closed states induced by 0.1–100 μM GMP·PPi (Fig. 3c and Extended Data Fig. 6b). This is consistent with previous reports that domain closure is required for triphosphate nucleotide binding[25,44] and reflects GMP·PPi binding through stabilization of the high-FRET closed conformation rather than an acceleration of domain closure (Extended Data Fig. 6c). The GMP·PPi-induced transitions also exhibited ligand-specific differences; complexes with the lower-efficacy ligand MOP (Fig. 3d and Extended Data Fig. 6f–h) showed heightened sensitivity to GMP·PPi (half-maximal effective concentration (EC_{50}) = 0.34 μM; 95% confidence interval (CI): 0.19–0.61) compared to those with DAMGO (EC_{50} = 1.53 μM; 95% CI: 0.44–5.3 μM) (Fig. 3d). This difference aligns with the ligand-dependent energetic biases for AHD closure, as evident from their conformational equilibria before nucleotide binding (Fig. 2a). Importantly, even at the highest GMP·PPi concentrations tested (≥10 μM), transitions to the basal (~0.77 FRET) state remained rare (Extended Data Figs. 6b,f and 7a,b), suggesting that receptor coupling restricts access to the fully closed conformation of the AHD regardless of nucleotide.

https://doi.org/10.1038/s41594-026-01893-6

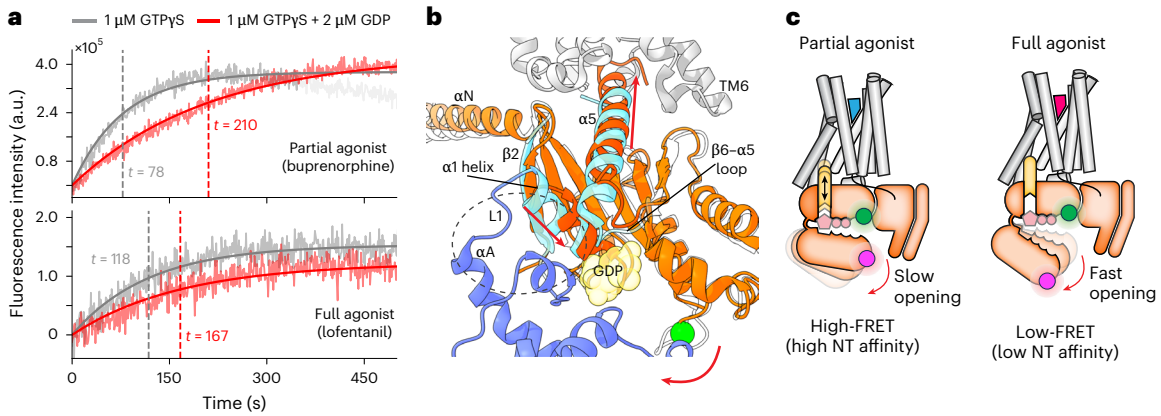


Fig. 4 | Linking AHD dynamics to ligand efficacy. a, GTPγS–BDP-FL binding to nucleotide-free μOR–G_i containing an unlabeled $Gα_iΔ6$-90C/238C α-subunit was monitored by fluorescence dequenching for LFT (bottom) and BUP (top). Normalized kinetic spectra in the absence (gray) and presence (red) of 2 μM GDP fit to a single exponential function (*t*, mean association time; dashed lines). **b**, $Gα_i$ α5 helix engaging the intracellular surface of μOR destabilizes the α1 helix and disrupts the interdomain interface (dashed outline) composed of αF, α1, L1 and the N-terminal portion of αA (PDB 1GP2, blue; PDB 7T2H, orange). **c**, Schematic of main FRET states and proposed connection to α5 insertion and nucleotide (NT) binding. Full agonists bias the conformational equilibrium toward an open state (right) with reduced nucleotide affinity, while partial agonists shift the G protein toward a state with greater AHD closure (left). This shift increases the energy required for nucleotide release, thus reducing the likelihood of progressing to the nucleotide-free complex.

Further analysis of individual smFRET traces (Extended Data Fig. 6d,g and Extended Data Fig. 7a,b) revealed stepwise transitions through a partially open, mid-FRET state (~0.4–0.5) within both DAMGO-bound and MOP-bound complexes (Fig. 3e and Extended Data Fig. 6h). GMP·PPi-induced stabilization of this intermediate was weaker in DAMGO-bound complexes, which, at this temporal resolution, maintained more apparent direct transitions between low-FRET and high-FRET states even at saturating nucleotide concentrations (Fig. 3e). However, synchronization analysis revealed a brief (1–2 frames) mid-FRET dwell during many of these domain separation events (Fig. 3f and Extended Data Fig. 6e). We also observed stepwise transitions in heterotrimeric G_i with GDP present (Extended Data Fig. 5d), aligning with a prior smFRET study that linked the partial domain separation in an intermediate-FRET state to an intermediate level of nucleotide affinity[21].

Together, these findings suggest a mechanism where nucleotide contacts are broken or formed progressively rather than all at once, providing a free-energy-efficient pathway for nucleotide exchange through a transient intermediate step[45,46]. One possible model is that this intermediate represents a conformation where the AHD has opened but the flexible switch III loop (containing the RLD probe at residue 238) remains transiently ordered by conserved 'triad' interactions[47] coordinating the GMP·PPi terminal phosphate before its full release. The similar accessibility of this transitional conformation in the nucleotide-free state across ligands (Fig. 2a) may allow for selective modulation of GDP release (that is, by tuning high-FRET state stability) without as drastically affecting GTP binding.

Discussion

We showed that opioid ligand efficacy extends beyond initial receptor–G protein coupling to include the modulation of G protein conformational equilibria within the fully formed signaling complex. These results demonstrate that the G protein conformation can be dynamically tuned by the GPCR, sampling a continuum of states rather than discrete 'off' or 'on' conformations (Fig. 2b). While these insights may be relevant to efforts to develop safer opioid analgesics[48–51], they also suggest a broader framework for how the interplay between receptor and effector conformational states can influence signaling response, which is important across GPCR targets[52,53].

Our findings reveal that ligand-dependent conformational changes propagate from the receptor to the engaged G protein, modulating its AHD across open, closed and transient intermediate states. Consistent with the loss of contacts upon separation of the Gα domains, our measurements showed that the high-FRET (closed) state corresponds to higher nucleotide affinity, while the low-FRET (open) state possesses reduced affinity (Fig. 3c,d). This aligns with recent complementary cryo-EM structures of μOR–G_i revealing ligand-dependent GDP-bound intermediates with distinct AHD conformations[54], as well as prior findings that mutations of the interdomain interface or hinge regions accelerate basal nucleotide exchange[25,40,55,56] and increased interdomain motion correlates with G protein activation[57–59]. The energetic bias toward AHD opening we observe in full agonist-bound complexes (Fig. 2a and Extended Data Fig. 3a) should reduce their nucleotide affinity, driven by the shift in the G protein conformational equilibria.

To test this, we measured GTPγS binding to nucleotide-free μOR–G_i complexes by fluorescence dequenching (Methods). BUP-occupied complexes exhibited 1.5-fold faster GTPγS binding than those bound to the full agonist LFT (Fig. 4a), consistent with extensive earlier evidence that higher-efficacy ligands reduce the nucleotide affinity of coupled G proteins[5,60–65]. Although this initially appears to contradict in vivo signaling patterns, measurements under more physiological conditions (that is, where both GDP and GTP are present) showed a reversal in binding kinetics (Fig. 4a), with GDP competition asymmetrically slowing GTPγS binding to BUP-bound complexes[66].

In the cytoplasm, where GTP is approximately tenfold more abundant than GDP, G protein activation is primarily limited by GDP release, as GTP loading occurs rapidly afterward. Full agonists promote AHD opening, facilitating GDP release and, therefore, efficient GTP binding. In contrast, partial agonists restrict open-state occupancy, favoring GDP retention or rebinding, which prolongs its residence time in the interdomain pocket. This competitively inhibits GTP binding and delays G protein activation, ultimately explaining why partial agonists exhibit lower signaling efficacy despite faster intrinsic GTPγS binding rates (Fig. 4a). The relative difference between ligands is also greater for GDP than for GTP binding, further suggesting that G protein dynamics are primarily selected to regulate the GDP release step, although opioid-dependent regulation of GTP exchange has also been recently reported.

At a structural level, these ligand-induced G protein conformational changes require allosteric communication spanning over 70 Å from the receptor's orthosteric site to the G protein AHD. Differences in G protein dynamics observed with different orthosteric ligands can be understood as alterations in the complementarity between the

binding surfaces where the RLD and AHD meet. While GPCR-mediated G protein activation is known to involve remodeling of the α5 helix in the Gα subunit[67–70], studies also link this helix to AHD opening[10,23,71], minimally through the α1 helix in the RLD[72,73] (Fig. 4b). The α1 helix directly connects to the AHD through the αA helix and helps to stabilize the inactive G protein conformation through conserved interdomain contacts with αF and the hinge region[74]. During GPCR engagement, α5 moves away from the nucleotide-binding pocket toward the intracellular vestibule of the receptor, causing rotation and partial disorder of α1. These rearrangements sterically disrupt the interdomain interface, opening the AHD and priming the ternary complex for GDP release[13,15,70] (Fig. 4b). In addition, the fact that the AHD is partially displaced from the RLD in the receptor-bound high-FRET state suggests that some steric disruption has already occurred. This 'preactivated' conformation may lower the barrier for GDP release during the early stages of ternary complex assembly, with the extent of this priming potentially varying across different G_i-coupled receptors.

smFRET and DEER studies of β2-adrenergic and μOR receptors have shown that full agonists promote greater outward movement of transmembrane helix 6 (TM6)[5,6], which expands the intracellular vestibule where the α5 helix binds. This TM6 displacement, along with other ligand-dependent changes to the receptor's cytosolic surface, may facilitate AHD opening by making it more energetically favorable for the G protein α5 to fully engage[15,75–77]. In contrast, partial agonists have been shown to induce less efficient α5 insertion[78], which could weaken α1-mediated disruption of the Gα interdomain interface and prolong the dwell time in the high-FRET, high-nucleotide-affinity state preceding GDP release (Fig. 4c). This mechanism helps explain an earlier observation that partial agonists at β2–G_s act to stabilize transient GDP-bound GPCR–G protein intermediates[5], which could function as kinetic traps retarding productive complex assembly and activation. As for the low-affinity open state, the similar low-FRET dwell times observed across opioid agonists (Fig. 2d) suggest that, once the AHD is fully open, ligand identity has minimal influence on its dynamics, possibly because the AHD is affixed against Gβ, as seen in a recent cryo-EM structure[14].

Unlike real-time insights from smFRET, resolution of the AHD in cryo-EM studies of GPCR–G protein complexes is limited by the conformational heterogeneity captured upon freezing[16,59]. As such, it may be unsurprising that structures with ligands of varying efficacies often show minimal differences in Gα[61,79,80], capturing primarily the lowest-energy conformations while even subtle changes at the interdomain interface can greatly alter domain separation dynamics[74]. Lipid bilayers have also been shown to promote AHD opening in $G\alpha_s$ independent of receptor engagement[81] and certain small molecules that target G proteins have been demonstrated to select for a specific state of the AHD, such as the G_q inhibitor YM-254890 (ref. 82). Interplay between such direct perturbations of G protein conformation and the ligand-dependent bias observed here may ultimately help to explain previously unappreciated signaling outcomes. Together, these findings point to the G protein itself as an additional locus through which ligand-specific signaling behavior can emerge, providing a mechanistic rationale for how certain opioid ligands could produce partial agonism with potentially fewer adverse effects.

Online content

Any methods, additional references, Nature Portfolio reporting summaries, source data, extended data, supplementary information, acknowledgements, peer review information; details of author contributions and competing interests; and statements of data and code availability are available at https://doi.org/10.1038/s41594-026-01893-6.

References

1. Pierce, K. L., Premont, R. T. & Lefkowitz, R. J. Seven-transmembrane receptors. *Nat. Rev. Mol. Cell Biol.* **3**, 639–650 (2002).
2. Hilger, D. The role of structural dynamics in GPCR-mediated signaling. *FEBS J.* **288**, 2461–2489 (2021).
3. Ghanouni, P. et al. Functionally different agonists induce distinct conformations in the G protein coupling domain of the β2 adrenergic receptor. *J. Biol. Chem.* **276**, 24433–24436 (2001).
4. Kofuku, Y. et al. Efficacy of the β_2-adrenergic receptor is determined by conformational equilibrium in the transmembrane region. *Nat. Commun.* **3**, 1045 (2012).
5. Gregorio, G. G. et al. Single-molecule analysis of ligand efficacy in β2AR–G-protein activation. *Nature* **547**, 68–73 (2017).
6. Zhao, J. et al. Ligand efficacy modulates conformational dynamics of the μ-opioid receptor. *Nature* **629**, 474–480 https://doi.org/10.1038/s41586-024-07295-2 (2024).
7. Sungkaworn, T. et al. Single-molecule imaging reveals receptor–G protein interactions at cell surface hot spots. *Nature* **550**, 543–547 (2017).
8. Lohse, M. J., Maiellaro, I. & Calebiro, D. Kinetics and mechanism of G protein-coupled receptor activation. *Curr. Opin. Cell Biol.* **27**, 87–93 (2014).
9. Huang, S. K. & Prosser, R. S. Dynamics and mechanistic underpinnings to pharmacology of class A GPCRs: an NMR perspective. *Am. J. Physiol. Cell Physiol.* **322**, C739–C753 (2022).
10. Van Eps, N. et al. Interaction of a G protein with an activated receptor opens the interdomain interface in the alpha subunit. *Proc. Natl Acad. Sci. USA* **108**, 9420–9424 (2011).
11. Rasmussen, S. G. F. et al. Crystal structure of the β2 adrenergic receptor–G_s protein complex. *Nature* **477**, 549–555 (2011).
12. Oldham, W. M. & Hamm, H. E. Heterotrimeric G protein activation by G-protein-coupled receptors. *Nat. Rev. Mol. Cell Biol.* **9**, 60–71 (2008).
13. Chung, K. Y. et al. Conformational changes in the G protein G_s induced by the β2 adrenergic receptor. *Nature* **477**, 611–615 (2011).
14. Zhang, M. et al. Cryo-EM structure of an activated GPCR–G protein complex in lipid nanodiscs. *Nat. Struct. Mol. Biol.* **28**, 258–267 (2021).
15. Hilger, D., Masureel, M. & Kobilka, B. K. Structure and dynamics of GPCR signaling complexes. *Nat. Struct. Mol. Biol.* **25**, 4–12 (2018).
16. Westfield, G. H. et al. Structural flexibility of the $G\alpha_s$ α-helical domain in the β2-adrenoceptor G_s complex. *Proc. Natl Acad. Sci. USA* **108**, 16086–16091 (2011).
17. Dohlman, H. & Jones, J. Signal activation and inactivation by the G helical domain: a long-neglected partner in G protein signaling. *Sci. Signal.* **5**, re2 (2012).
18. Warner, D. R. & Weinstein, L. S. A mutation in the heterotrimeric stimulatory guanine nucleotide binding protein α-subunit with impaired receptor-mediated activation because of elevated GTPase activity. *Proc. Natl Acad. Sci. USA* **96**, 4268–4272 (1999).
19. Grishina, G. & Berlot, C. H. A surface-exposed region of $G_s\alpha$ in which substitutions decrease receptor-mediated activation and increase receptor affinity. *Mol. Pharmacol.* **57**, 1081–1092 (2000).
20. Yao, X.-Q. et al. Dynamic coupling and allosteric networks in the α subunit of heterotrimeric G proteins. *J. Biol. Chem.* **291**, 4742–4753 (2016).
21. Zhu, Y., Zhang, L., Zhang, X. C. & Zhao, Y. Structural dynamics of $G_i\alpha$ protein revealed by single molecule FRET. *Biochem. Biophys. Res. Commun.* **491**, 603–608 (2017).
22. Galés, C. et al. Probing the activation-promoted structural rearrangements in preassembled receptor–G protein complexes. *Nat. Struct. Mol. Biol.* **13**, 778–786 (2006).
23. Dror, R. O. et al. Structural basis for nucleotide exchange in heterotrimeric G proteins. *Science* **348**, 1361–1365 (2015).
24. Ceruso, M. A., Periole, X. & Weinstein, H. Molecular dynamics simulations of transducin: interdomain and front to back communication in activation and nucleotide exchange. *J. Mol. Biol.* **338**, 469–481 (2004).

25. Markby, D. W., Onrust, R. & Bourne, H. R. Separate GTP binding and GTPase activating domains of a Gα subunit. *Science* **262**, 1895–1901 (1993).
26. Papasergi-Scott, M. M. et al. Time-resolved cryo-EM of G-protein activation by a GPCR. *Nature* **629**, 1182–1191 (2024).
27. Altman, R. B. et al. Cyanine fluorophore derivatives with enhanced photostability. *Nat. Methods* **9**, 68–71 (2012).
28. Grimm, J. B. et al. Optimized red-absorbing dyes for imaging and sensing. *J. Am. Chem. Soc.* **145**, 23000–23013 (2023).
29. Medkova, M., Preininger, A. M., Yu, N.-J., Hubbell, W. L. & Hamm, H. E. Conformational changes in the amino-terminal helix of the G protein α_{i1} following dissociation from Gβγ subunit and activation. *Biochemistry* **41**, 9962–9972 (2002).
30. Neilan, C. L. et al. Characterization of the complex morphinan derivative BU72 as a high efficacy, long-lasting mu-opioid receptor agonist. *Eur. J. Pharmacol.* **499**, 107–116 (2004).
31. Hein, P., Frank, M., Hoffmann, C., Lohse, M. J. & Bünemann, M. Dynamics of receptor/G protein coupling in living cells. *EMBO J.* **24**, 4106–4114 (2005).
32. Galés, C. et al. Real-time monitoring of receptor and G-protein interactions in living cells. *Nat. Methods* **2**, 177–184 (2005).
33. Bünemann, M., Frank, M. & Lohse, M. J. G_i protein activation in intact cells involves subunit rearrangement rather than dissociation. *Proc. Natl Acad. Sci. USA* **100**, 16077–16082 (2003).
34. Nikolaev, V. O., Hoffmann, C., Bünemann, M., Lohse, M. J. & Vilardaga, J.-P. Molecular basis of partial agonism at the neurotransmitter α_{2A}-adrenergic receptor and G_i-protein heterotrimer. *J. Biol. Chem.* **281**, 24506–24511 (2006).
35. Lohse, M. J. et al. Kinetics of G-protein-coupled receptor signals in intact cells. *Br. J. Pharmacol.* **153**, S125–S132 (2008).
36. Moore, M. N. et al. Designing allosteric modulators to change GPCR G protein subtype selectivity. *Nature* **648**, 229–238 (2025).
37. Furness, S. G. B. et al. Ligand-dependent modulation of G protein conformation alters drug efficacy. *Cell* **167**, 739–749 (2016).
38. Wall, M. A. et al. The structure of the G protein heterotrimer $G_i\alpha_1\beta_1\gamma_2$. *Cell* **83**, 1047–1058 (1995).
39. Liu, X. et al. Structural insights into the process of GPCR–G protein complex formation. *Cell* **177**, 1243–1251.e12 (2019).
40. Remmers, A. E., Engel, C., Liu, M. & Neubig, R. R. Interdomain interactions regulate GDP release from heterotrimeric G proteins. *Biochemistry* **38**, 13795–13800 (1999).
41. Dudzinska, W., Lubkowska, A., Dolegowska, B., Safranow, K. & Jakubowska, K. Adenine, guanine and pyridine nucleotides in blood during physical exercise and restitution in healthy subjects. *Eur. J. Appl. Physiol.* **110**, 1155–1162 (2010).
42. Lefevre, T. J. et al. Stabilization of interdomain interactions in G protein α subunits as a determinant of $G\alpha_i$ subtype signaling specificity. *J. Biol. Chem.* **300**, 107211 (2024).
43. Zhang, B., Zhang, Y., Shacter, E. & Zheng, Y. Mechanism of the guanine nucleotide exchange reaction of Ras GTPase: evidence for a GTP/GDP displacement model. *Biochemistry* **44**, 2566–2576 (2005).
44. Du, Y. et al. Assembly of a GPCR–G protein complex. *Cell* **177**, 1232–1242 (2019).
45. Toyama, Y. et al. Dynamic regulation of GDP binding to G proteins revealed by magnetic field-dependent NMR relaxation analyses. *Nat. Commun.* **8**, 14523 (2017).
46. Sun, X., Singh, S., Blumer, K. J. & Bowman, G. R. Simulation of spontaneous G protein activation reveals a new intermediate driving GDP unbinding. *eLife* **7**, e38465 (2018).
47. Knight, K. M. et al. A universal allosteric mechanism for G protein activation. *Mol. Cell* **81**, 1384–1396 (2021).
48. Cowan, A. Buprenorphine: new pharmacological aspects. *Int. J. Clin. Pract. Suppl.* (133), 3–8 (2003).
49. Gillis, A., Sreenivasan, V. & Christie, M. J. Intrinsic efficacy of opioid ligands and its importance for apparent bias, operational analysis, and therapeutic window. *Mol. Pharmacol.* **98**, 410–424 (2020).
50. Gillis, A. et al. Low intrinsic efficacy for G protein activation can explain the improved side effect profiles of new opioid agonists. *Sci. Signal.* **13**, eaaz3140 (2020).
51. Stahl, E. L. & Bohn, L. M. Low intrinsic efficacy alone cannot explain the improved side effect profiles of new opioid agonists. *Biochemistry* **61**, 1923–1935 (2022).
52. Lipworth, B. J. & Grove, A. Evaluation of partial β-adrenoceptor agonist activity. *Br. J. Clin. Pharmacol.* **43**, 9–14 (1997).
53. Kenakin, T. New concepts in pharmacological efficacy at 7TM receptors: IUPHAR review 2. *Br. J. Pharmacol.* **168**, 554–575 (2013).
54. Khan, S. et al. Structural snapshots capture nucleotide release at the μ-opioid receptor. *Nature* **648**, 755–763 (2025).
55. Kalogriopoulos, N. A. et al. Receptor tyrosine kinases activate heterotrimeric G proteins via phosphorylation within the interdomain cleft of $G\alpha_i$. *Proc. Natl Acad. Sci. USA* **117**, 28763–28774 (2020).
56. Marin, E. P. et al. The function of interdomain interactions in controlling nucleotide exchange rates in transducin. *J. Biol. Chem.* **276**, 23873–23880 (2001).
57. Jones, J. C. et al. The crystal structure of a self-activating G protein α subunit reveals its distinct mechanism of signal initiation. *Sci. Signal.* **4**, ra8 (2011).
58. Jones, J. C., Jones, A. M., Temple, B. R. S. & Dohlman, H. G. Differences in intradomain and interdomain motion confer distinct activation properties to structurally similar Gα proteins. *Proc. Natl Acad. Sci. USA* **109**, 7275–7279 (2012).
59. Abdulaev, N. G. et al. The receptor-bound 'empty pocket' state of the heterotrimeric G-protein α-subunit is conformationally dynamic. *Biochemistry* **45**, 12986–12997 (2006).
60. Roberts, D. J., Lin, H. & Strange, P. G. Mechanisms of agonist action at D2 dopamine receptors. *Mol. Pharmacol.* **66**, 1573–1579 (2004).
61. Su, M. et al. Structures of β1-adrenergic receptor in complex with G_s and ligands of different efficacies. *Nat. Commun.* **13**, 4095 (2022).
62. Breivogel, C. S., Selley, D. E. & Childers, S. R. Cannabinoid receptor agonist efficacy for stimulating [^{35}S]GTPγS binding to rat cerebellar membranes correlates with agonist-induced decreases in GDP affinity. *J. Biol. Chem.* **273**, 16865–16873 (1998).
63. Zhang, Q., Okamura, M., Guo, Z.-D., Niwa, S. & Haga, T. Effects of partial agonists and Mg^{2+} ions on the interaction of M2 muscarinic acetylcholine receptor and G protein $G\alpha_{i1}$ subunit in the M2–$G\alpha_{i1}$ fusion protein. *J. Biochem.* **135**, 589–596 (2004).
64. Seifert, R., Gether, U., Wenzel-Seifert, K. & Kobilka, B. K. Effects of guanine, inosine, and xanthine nucleotides on β2-adrenergic receptor/G_s interactions: evidence for multiple receptor conformations. *Mol. Pharmacol.* **56**, 348–358 (1999).
65. Selley, D. E., Sim, L. J., Xiao, R., Liu, Q. & Childers, S. R. μ-Opioid receptor-stimulated guanosine-5′-*O*-(γ-thio)-triphosphate binding in rat thalamus and cultured cell lines: signal transduction mechanisms underlying agonist efficacy. *Mol. Pharmacol.* **51**, 87–96 (1997).
66. Harrison, C. & Traynor, J. R. The [^{35}S]GTPγS binding assay: approaches and applications in pharmacology. *Life Sci.* **74**, 489–508 (2003).
67. Herrmann, R. et al. Sequence of interactions in receptor–G protein coupling. *J. Biol. Chem.* **279**, 24283–24290 (2004).
68. Oldham, W. M., van Eps, N., Preininger, A. M., Hubbell, W. L. & Hamm, H. E. Mechanism of the receptor-catalyzed activation of heterotrimeric G proteins. *Nat. Struct. Mol. Biol.* **13**, 772–777 (2006).

69. Kapoor, N., Menon, S. T., Chauhan, R., Sachdev, P. & Sakmar, T. P. Structural evidence for a sequential release mechanism for activation of heterotrimeric G proteins. *J. Mol. Biol.* **393**, 882–897 (2009).
70. Kaya, A. I. et al. A conserved hydrophobic core in $G\alpha_{i1}$ regulates G protein activation and release from activated receptor. *J. Biol. Chem.* **291**, 19674–19686 (2016).
71. Alexander, N. S. et al. Energetic analysis of the R*–G complex links the α5 helix to GDP release and domain opening. *Nat. Struct. Mol. Biol.* **21**, 56–63 (2014).
72. Teng, X. et al. Structural insights into G protein activation by D1 dopamine receptor. *Sci. Adv.* **8**, eabo4158 (2022).
73. Flock, T. et al. Universal allosteric mechanism for Gα activation by GPCRs. *Nature* **524**, 173–179 (2015).
74. Sun, D. et al. Probing $G\alpha_{i1}$ protein activation at single-amino acid resolution. *Nat. Struct. Mol. Biol.* **22**, 686–694 (2015).
75. Lee, S., Nivedha, A. K., Tate, C. G. & Vaidehi, N. Dynamic role of the G protein in stabilizing the active state of the adenosine A_{2A} receptor. *Structure* **27**, 703–712 (2019).
76. Huang, S. K. et al. Delineating the conformational landscape of the adenosine A_{2A} receptor during G protein coupling. *Cell* **184**, 1884–1894 (2021).
77. Heydenreich, F. M. et al. Molecular determinants of ligand efficacy and potency in GPCR signaling. *Science* **382**, eadh1859 (2023).
78. Kim, K. et al. β2-adrenoceptor ligand efficacy is tuned by a two-stage interaction with the $G\alpha_s$ C terminus. *Proc. Natl Acad. Sci. USA* **118**, e2017201118 (2021).
79. Xu, P. et al. Structural insights into the lipid and ligand regulation of serotonin receptors. *Nature* **592**, 469–473 (2021).
80. Qu, Q. et al. Insights into distinct signaling profiles of the μOR activated by diverse agonists. *Nat. Chem. Biol.* **19**, 423–430 (2023).
81. Huang, S. K. et al. Mapping the conformational landscape of the stimulatory heterotrimeric G protein. *Nat. Struct. Mol. Biol.* **30**, 502–511 https://doi.org/10.1038/s41594-023-00957-1 (2023).
82. Todd, T. D. et al. Stabilization of interdomain closure by a G protein inhibitor. *Proc. Natl Acad. Sci. USA* **121**, e2311711121 (2024).

Publisher's note Springer Nature remains neutral with regard to jurisdictional claims in published maps and institutional affiliations.

Open Access This article is licensed under a Creative Commons Attribution-NonCommercial-NoDerivatives 4.0 International License, which permits any non-commercial use, sharing, distribution and reproduction in any medium or format, as long as you give appropriate credit to the original author(s) and the source, provide a link to the Creative Commons licence, and indicate if you modified the licensed material. You do not have permission under this licence to share adapted material derived from this article or parts of it. The images or other third party material in this article are included in the article's Creative Commons licence, unless indicated otherwise in a credit line to the material. If material is not included in the article's Creative Commons licence and your intended use is not permitted by statutory regulation or exceeds the permitted use, you will need to obtain permission directly from the copyright holder. To view a copy of this licence, visit http://creativecommons.org/licenses/by-nc-nd/4.0/.

© The Author(s) 2026

Methods

Minimal cysteine $G\alpha_i$ expression, purification and labeling

The R90C and E238C substitutions were introduced into a previously published minimal cysteine background (C3S;C66A;C214S;C350S;C 325A;C351I) of human $G\alpha_{i1}$ containing an N-terminal 6×His tag before a rhinovirus 3C protease site. This construct ($G\alpha_{i1}\Delta$6-90C/238C)[10] was expressed in BL21(DE3) cells (Sigma-Aldrich, CMC0014) using pET28a and purified as previously described[83]. Briefly, cells grown in Terrific Broth were induced with 0.5 mM IPTG at an OD_{600} of 0.6 and harvested after 15–20 h at room temperature. The harvested cells were resuspended in lysis buffer (50 mM HEPES pH 7.4, 100 mM NaCl, 1 mM $MgCl_2$, 50 µM GDP, 5 mM β-mercaptoethanol, 5 mM imidazole, lysozyme and protease inhibitors) and disrupted by sonication. Intact cells and cell debris were removed by centrifugation and $G\alpha_i$ was purified from the supernatant using Ni-NTA resin. The protein was eluted using 200 mM imidazole in lysis buffer and dialyzed with 1:1,000 w/w 3C protease at 4 °C overnight to cleave the histidine tag. The 3C protease, cleaved histidine tag and unreacted protein were removed using fresh Ni-NTA and the flowthrough containing purified Gα was concentrated and polished using size-exclusion chromatography (SEC) on a Superdex 200 10/300 GL column (Cytiva) in G protein buffer (20 mM HEPES pH 7.4, 100 mM NaCl, 1 mM $MgCl_2$, 20 µM GDP and 100 uM TCEP). For preparation of His-tagged $G\alpha_i$, the Ni-NTA eluate was concentrated and further purified using SEC without an intervening 3C cleavage step. The R144A substitution was introduced into $G\alpha_{i1}\Delta$6-90C/238C through quickchange-style mutagenesis using primeSTAR Max premix (Takara Bio, 4045A) and forward primer 5′-CCTGTTTCAACAGATCCGCGGAGTACCAGCTTAATGATTCTGC-3′ with its complementary reverse primer. The resulting protein was purified with an intact His tag. Aliquots of purified $G\alpha_i$ were flash-frozen in liquid nitrogen at a concentration of approximately 200 µM in 20% glycerol as a cryoprotectant. WT $G\alpha_i$ for control experiments was expressed and purified like the minimal cysteine constructs.

For site-specific labeling, fluorophores were attached to C90 and C238 in $G\alpha_i\Delta$6-90C/238C under conditions designed to minimize off-site conjugation (Extended Data Fig. 1a). Aliquots of frozen, purified Gα were brought to room temperature and diluted to a concentration of 30 µM in G protein buffer containing 50 µM GDP. Maleimide-conjugated LD555 (Lumidyne Technologies) and JFX673-peg_4 (Janelia Fluor) were added simultaneously, each at a twofold molar excess, and incubated at room temperature for 0.5 h. The reaction was quenched by 5 mM L-cysteine (Sigma) and labeled protein was purified from the unreacted dyes using a Superdex 200 column in buffer containing 20 mM HEPES pH 7.4, 100 mM NaCl, 1 mM $MgCl_2$, 20 µM GDP and 100 µM TCEP. SEC-pure, dye-labeled $G\alpha_i$ was concentrated and flash-frozen at approximately 60 µM for future use.

Purification of Gβγ

Gβγ heterodimer was expressed in *Trichoplusia ni* (Hi-5) cells (Expression Systems, 94011S) using a baculovirus generated by the BestBac (Expression Systems) method and purified as described previously[23]. Briefly, we used a single virus containing the genes for both the human $G\beta_1$ and $G\gamma_2$ subunits. An N-terminal 6×His tag followed by a 3C protease site was contained in the sequence of Gβ to be used for Ni affinity purification. Hi-5 cells were infected at a density of 3×10^6 cells per ml and incubated at 27 °C for 48 h. Cell pellets were lysed in 10 mM Tris pH 7.5, 5 mM β-mercaptoethanol and protease inhibitors and Gβγ heterodimer was extracted from the membrane fraction using a dounce homogenizer in solubilization buffer containing 20 mM HEPES pH 7.4, 100 mM NaCl, 1.0% sodium cholate, 0.05% dodecylmaltoside (DDM; Anatrace), 5 mM β-mercaptoethanol and protease inhibitors. After removing insoluble debris, the protein was washed with a solubilization buffer in batch and gradually exchanged from sodium cholate to 0.1% DDM on Ni-NTA resin. The eluate was dialyzed with 3C protease to cleave the histidine tag as described above for $G\alpha_i$. Cleaved Gβγ was dephosphorylated and diluted to 50 mM NaCl before further purification on a MonoQ 10/100 GL column (GE Healthcare) using a linear gradient of NaCl (50–250 mM in 20 mM HEPES pH 7.4, 0.02% DDM and 100 µM TCEP). The main peak containing prenylated Gβγ was dialyzed into 20 mM HEPES pH 7.4, 100 mM NaCl and 0.02% DDM and flash-frozen in liquid nitrogen at a concentration of 150 µM with 20% glycerol as a cryoprotectant. WT G_i heterotrimer ($G\alpha_{i1}\beta_1\gamma_2$) from Hi-5 cells was prepared similarly through coinfection with the Gβγ virus and a second virus containing the human $G\alpha_{i1}$ sequence. Expression and purification then proceeded in the same manner but with the addition of 30 µM GDP and 100 µM $MgCl_2$ to lysis and purification buffers. The main peak from MonoQ containing G_{i1} heterotrimer was dialyzed into a final buffer of 20 mM HEPES pH 7.4, 100 mM NaCl, 0.05% DDM, 100 µM TCEP, 20 µM GDP and 1 mM $MgCl_2$ and flash-frozen at ~200 µM with 20% glycerol.

Formation of dye-labeled G_i heterotrimer

Purified Gβγ heterodimer was exchanged into buffer containing 20 mM HEPES pH 7.4, 100 mM NaCl, 1 mM $MgCl_2$, 50 µM GDP and 100 µM TCEP using a centrifugal protein concentrator (30-kDa molecular weight cutoff (MWCO); Thermo Scientific) and mixed with approximately 0.25 molar equivalents of dye-labeled $G\alpha_i\Delta$6-90C/238C–6×His (2.5 µM $G\alpha_i$ final concentration). Buffer exchange was performed until the final concentration of DDM during heterotrimer formation was much lower than the critical micellar concentration. After incubation at room temperature for 0.5 h, unbound Gβγ heterodimers were removed coincident with surface immobilization for smFRET imaging by pulling down the heterotrimer on microscope slides coated in anti-His epitope tag antibodies.

Purification of µOR

Mouse µOR was expressed in *Sf9* insect cells (Expression Systems, 940-001S) using the baculovirus method (BestBac, Expression Systems) in the presence of the opioid antagonist naloxone (Sigma-Aldrich). We used a modified *Mus musculus* sequence containing an N-terminal Flag tag and an 8×His tag in front of a rhinovirus 3C protease site on the C terminus. µOR was expressed and purified in the presence of 10 µM naloxone as previously described[84]. Briefly, *Sf9* cells were infected at a density of 4×10^6 cells per ml and incubated for 48 h at 27 °C. Cell membranes were solubilized in DDM and CHAPS (Anatrace) and purified by immobilized metal affinity chromatography using Ni-NTA resin. The eluate was loaded onto M1 anti-Flag immunoaffinity resin and gradually exchanged into a buffer containing naloxone, 0.01% lauryl maltose neopentyl glycol (L-MNG; Anatrace) and 0.001% cholesterol hemisuccinate (CHS; Steraloids). The receptor was further purified on SEC in a buffer containing no ligand, 25 mM HEPES pH 7.4, 100 mM NaCl, 0.02% L-MNG and 0.002% CHS. The peak containing the now unliganded µOR (Extended Data Fig. 1d, dashed line) was concentrated to ~100 µM, supplemented with 20% glycerol and flash-frozen for later use.

Assembly of µOR–G_i

To prepare µOR–G_i ternary complexes for smFRET, µOR was equilibrated in a 5–10 molar excess of opioid agonist for 10 min at room temperature. After preincubation of untagged $G\alpha_i$ and Gβγ on ice for 30 min, they were mixed with liganded receptor at a 1:1.2:1 ($G\alpha_i$:Gβγ:µOR) molar ratio. The final concentration of receptor during complexing was ~2.5 µM and the buffer was adjusted to contain 20 mM HEPES pH 7.4, 100 mM NaCl, 0.01% L-MNG, 0.001% CHS, 100 µM TCEP, 50 µM GDP and 1 mM $MgCl_2$. Complex assembly progressed for 1 h at room temperature to reach steady state, after which 25 mU per ml apyrase (New England Biolabs) was added before incubation overnight at 4 °C. The apyrase-stabilized complex was supplemented with 2 mM $CaCl_2$ and loaded onto an M1 anti-Flag immunoaffinity column at room temperature. The column was washed with 20 column volumes of complex buffer (20 mM HEPES pH 7.4, 100 mM NaCl, 0.01% L-MNG,

0.001% CHS and 1–10 μM ligand) containing 2 mM $CaCl_2$ before the protein was eluted using 200 μg ml^{-1} Flag peptide (DYKDDDDK) and 2 mM EDTA. The eluate was further purified using a room temperature Superdex 200 10/300 SEC column in complex buffer containing 0.1–1 μM ligand. Peak fractions corresponding to monodispersed μOR–G_i were concentrated to ~3 μM and supplemented with 20% glycerol before flash-freezing in liquid nitrogen. Single-use aliquots were stored at −80 °C until imaging. Nearly identical apparent FRET efficiency distributions were obtained using complexes that were not frozen (data not shown). Given that the unliganded μOR–G_i complex showed reduced stability at room temperature, all chromatography and sample preparation steps for the apo complex were performed at 4 °C.

Purification and assembly of labeled NTSR1–G_i

Full-length human NTSR1 was expressed and purified as previously described[85]. In brief, an NTSR1 sequence modified with an N-terminal Flag tag followed by an 8×His tag was expressed in *Sf9* cells (Expression Systems, 94-001S) using a baculovirus. Solubilized cells were purified using sequential Ni-NTA, anti-Flag and SEC chromatography into a final buffer containing 20 mM HEPES, pH 7.4, 100 mM NaCl, 0.0025% L-MNG, 0.00025% CHS and 0.1 μM $NTS_{8–13}$ (acetate salt; Sigma). Peak fractions were concentrated to 200 μM, flash-frozen and stored at −80 °C.

Ternary complexes of NTSR1–G_i were assembled and purified as described for μOR above with a few modifications. Purified NTSR1 in 0.1 μM $NTS_{8–13}$ was loaded onto an anti-Flag column and exchanged into different orthosteric ligands (NTR1-17 or CGX-1160) by washing for 0.5 h (~15 column volumes) at room temperature with buffer containing 1 μM of the new ligand and 20 mM HEPES pH 7.4, 100 mM NaCl, 0.0025% L-MNG and 0.00025% CHS. Flag peptide and EDTA were removed from the eluate using a desalting spin column (7-kDa MWCO; Thermo Scientific) before the NTSR1 was concentrated and used for complexing. To couple to the receptor, labeled $G\alpha_i$Δ6-90/238C and Gβγ were first assembled into a heterotrimer as described above and were mixed with NTSR1 in an ~1:1 ratio following incubation. Complexing and SEC purification then progressed as for liganded μOR–G_i using buffers containing NTSR1 ligands.

GTP turnover assays

Analysis of GTP turnover was performed using a modified GTPase-Glo assay (Promega) as described previously[5]. We started the reaction by mixing 0.25 μM purified, unliganded or ligand-bound μOR or NTSR1 and G_i protein in an assay buffer containing 20 mM HEPES pH 7.5, 100 mM NaCl, 0.01% L-MNG, 0.001% CHS, 100 μM TCEP, 10 mM $MgCl_2$, 20 μM GDP, 10 μM GTP and saturating concentrations of receptor ligands (200 μM unless otherwise noted; LFT, 20 μM). After incubation for 7.5 min for μOR and 30 min for NTSR1, reconstituted GTPase-Glo reagent was added to the reaction and incubated for 30 min at room temperature with 5 μM ADP. Luminescence was measured after the addition of detection reagent and incubation for 10 min at room temperature using a Revvity Perk and Elmer MicroBeta2 plate reader. Measurements were performed in triplicate on the same plate and reported as the mean relative light units normalized to DAMGO or $NTS_{8–13}$ (Fig. 1b and Extended Data Fig. 3b). Ligand efficacy profiles were determined from the GTP turnover activity stimulated by μOR or NTSR1 using Δ6-90C/238C and WT $G\alpha_i$ constructs, respectively. Basal G_i-dependent GTP turnover was measured using 0.5 μM heterotrimer in buffer without any receptor and a 45-min incubation period. Data distributions were assumed to be normal but this was not tested.

smFRET measurements

Data were acquired using a lab-built prism-based TIRF microscope. $G\alpha_i$-Δ6-90/238C labeled with LD555 (donor) and JFX673-peg_4 (acceptor) was excited using a 532-nm solid-state laser (Coherent OBIS LS laser) set to 40 mW. Photons emitted from LD555 and JFX673 were collected through a ×60 (numerical aperture: 1.27) water-immersion objective (Nikon) and split onto two cooled electron-multiplying charge-coupled device cameras (Andor iXon Ultra 888) connected by a 640-nm dichroic mirror (ZT640rdc, Chroma) housed in a TwinCam (Cairn). All imaging was performed at 19 °C and videos were recorded with Andor Solis (i) software (Andor) at a 50-ms time resolution (20 fps). Microfluidic chambers for smFRET imaging were constructed from passivated quartz slides and coverslips using a modified protocol from Ha et al.[86]. Briefly, aminated glass surfaces passivated with mPEG-SVA (MW 5,000; Laysan Bio) doped with 0.6% w/w biotin-PEG-SVA (MW 5,000; Laysan Bio) were exposed to two additional rounds of passivation reactions using only mPEG-SVA.

For experiments with receptor–G_i ternary complexes, passivated imaging chambers were incubated for 5 min with 0.2 mg ml^{-1} NeutrAvidin (Thermo Scientific), followed by 5 min with 25 nM biotinylated anti-Flag M1 Fab fragment. Unbound M1 Fab and NeutrAvidin were washed out using imaging buffer (20 mM HEPES pH 7.5, 100 mM NaCl, 0.01% L-MNG, 0.001% CHS and 2 mM $CaCl_2$). Fluorophore-labeled μOR–G_i and NTSR1–G_i complexes were filtered using a 0.22-μm PVDF membrane (Millipore Sigma) and loaded onto the microscope slide at 200 pM by pulling down the N-terminal Flag tag on the receptor. Unbound complexes were washed out at an immobilization density of ~0.1 molecules per μm^2. All experiments were performed in imaging buffer containing saturating concentrations of tested ligands and without enzymatic oxygen scavenging. Measurements of each condition collected on different days using independent chambers were aggregated, with total molecule counts for each condition reported in the figures or legends.

For smFRET of basal G_i heterotrimer, NeutrAvidin-coated chambers were incubated for 5 min with 0.02 mg ml^{-1} biotinylated anti-mouse IgG1 antibody (BioLegend, 406603; 1:25 dilution) followed by 5 min with 0.02 mg ml^{-1} mouse anti-His epitope tag antibody (Qiagen, 34660; 1:50 dilution). Purified, LD555/JFX673-peg_4-labeled G_i with an uncleaved N-terminal 6×His tag on the α subunit was loaded onto the microscope slide at ~200 pM and measured in imaging buffer containing 30 μM GDP, 1 mM $MgCl_2$ and 100 μM TCEP. The procedure for anti-His tag immobilization was reported previously[87,88] and is specific. Nucleotide-free measurements were obtained by exchanging the heterotrimer into buffer without GDP on the surface for 30 min before imaging.

smFRET data analysis

Fluorescence time trajectories of single molecules were extracted from the videos and processed using a custom software suite implemented in MATLAB that is available on GitHub. Donor traces were scaled by a constant factor (γ) to account for the apparent unequal fluorophore brightnesses, calculated as $\gamma = \Delta I_A/\Delta I_D$, where ΔI_A and ΔI_D are the changes in donor and acceptor intensity after acceptor photobleaching, respectively[89]. FRET trajectories were calculated as $(1 + (\gamma I_D/I_A))^{-1}$, where I_D and I_A are the background-corrected donor and acceptor fluorescence intensities at each frame. Traces lasting at least 0.5 s and exhibiting single-step donor and acceptor photobleaching and overall anticorrelated donor and acceptor intensities were manually selected for further analysis. Stable low-FRET traces with FRET close to the donor-leakage background were excluded. The selected datasets had a mean signal-to-noise ratio (mean/s.d. of the total fluorescence intensity before photobleaching) of ~11 across all samples. Population histograms summed over the first 3 s of the selected FRET traces were fit to a mixture of 3–4 Gaussian functions in Python using sci-kit learn (version 1.3.2) to derive the state mean FRET values and occupancies. Initial component centers were estimated from the observed distributions, informed by *k*-means-initialized fits of the full agonists. Errors for the Gaussian mixtures and state occupancies were calculated from 1,000 bootstrap samples of the FRET traces.

FRET traces were idealized using a two-state or three-state HMM using vbFRET[90] (2012-12-09 release; default settings). The idealized

FRET traces (viterbi) were clustered using a Gaussian mixture model (GMM) to remove overfitting of fluctuations within the same FRET state and the resulting corrected state sequences were used to calculate transition density plots from transitions corresponding to $\Delta FRET_{ideal} > 0.1$. The number of states k for each condition was determined on the basis of the lowest value for which a $k+1$ state HMM fit did not change the clusters in a transition density plot of the uncorrected traces. For three-state fits, vbFRET camera-blur correction was enabled. To explore the exchange kinetics between the fully open and closed FRET states within μOR–G_i, the state sequences resulting from a two-state HMM and Gaussian mixture fit were concatenated ('stitched') and the dwell times in each state were extracted from the change points. Population dwell time distributions were calculated using a kernel density estimate (Gaussian kernel; bandwidth determined by Scott's rule), which was normalized to reflect the frequency of dwells in time bins along the x axis[91]. The mean lifetime in each state was estimated as the integral of the normalized Kaplan–Meier estimate of the dwell time survival curves restricted to <25 s for all ligands. Dwell times and their distributions are reported as the mean ± s.d. from 100 bootstrap samples of the idealized FRET traces, where the resampling probability of each trace is weighted by its relative duration[92]. Because each bootstrapped sample has a different randomly selected order of traces, this source of variability is averaged over and reflected in the reported errors.

Synchronization plots of the high-to-low transitions in DAMGO–μOR–G_i were calculated from clustering the viterbi paths to two-states and selecting transitions from above to below the intermediate state center (~0.45). While kinetics were analyzed with only γ correction, conversions of FRET efficiency to relative interdye distances used additional corrections for channel crosstalk and direct acceptor excitation, as outlined by Hellenkamp et al.[93]. Visualizations of the smFRET data were performed using custom scripts in Python (version 3.12).

BODIPY (BDP)–GTPγS binding assay

Binding of GTPγS–BDP-FL (Jena Bioscience) to nucleotide-free μOR–G_i complexes was measured as previously described[94]. Briefly, complexes of ligand-bound μOR, unlabeled $G\alpha_i$-Δ6-90/238C and Gβγ were purified by anti-Flag and added at a final concentration of 500 nM to a 500-μl quartz cuvette containing 1 μM GTPγS–BDP-FL. Fluorescence was recorded at 512 nm (495 nm excitation) for 600 s at room temperature using a Fluorolog spectrophotometer (HORIBA) and Horiba FluorEssence with magnetic stirring. All experiments were performed in a buffer containing saturating ligands and 20 mM HEPES pH 7.4, 100 mM NaCl, 0.01% L-MNG, 0.001% CHS, 2 mM $MgCl_2$ and 100 μM TCEP. Mean association times for GTPγS–BDP-FL binding were calculated from resulting kinetic spectra by fitting a pseudo-first-order association function using nonlinear least squares in Python. Data were background-corrected using the mean of the first ten time points. We note that the C325A substitution contained in the Δ6 cysteine construct reportedly affects the rate of spontaneous GDP release but not GTP binding[95].

Statistics and reproducibility

No statistical method was used to predetermine sample size. No data were excluded from the analyses; the experiments were not randomized; the investigators were not blinded to allocation during experiments and outcome assessment. Reproducibility of the single-molecule data was assessed across at least two independent experiments on different days with different imaging chambers. Biological replication (separate protein preparations starting from expression) was confirmed for the LFT complex. Sample sizes are reported in the figures or legends as the pooled number of molecules (n) observed for each condition. For bootstrap analysis, individual molecules were treated as the observational unit and resampled with replacement, preserving all FRET observations associated with each selected molecule. This procedure estimates uncertainty in the molecular state distributions arising from the finite number of molecules sampled and variation among molecules. Parametric curve fits and linear regression were performed in Python using SciPy (version 1.11.4).

Reporting summary

Further information on research design is available in the Nature Portfolio Reporting Summary linked to this article.

Data availability

Raw single-molecule traces and idealized trajectories needed to evaluate the conclusions are available through Zenodo (https://doi.org/10.5281/zenodo.22018761)[96]. Source data are provided with this paper.

Code availability

The custom MATLAB code used to process the smFRET data is available on Github (https://github.com/JonathanDeutsch/Freton).

References

83. Seven, A. B. et al. Structures of Gα proteins in complex with their chaperone reveal quality control mechanisms. *Cell Rep.* **30**, 3699–3709 (2020).
84. Huang, W. et al. Structural insights into μ-opioid receptor activation. *Nature* **524**, 315–321 (2015).
85. Huang, W. et al. Structure of the neurotensin receptor 1 in complex with β-arrestin 1. *Nature* **579**, 303–308 (2020).
86. Ha, T. et al. Initiation and re-initiation of DNA unwinding by the *Escherichia coli* Rep helicase. *Nature* **419**, 638–641 (2002).
87. Chen, W., Lu, W., Wolynes, P. G. & Komives, E. A. Single-molecule conformational dynamics of a transcription factor reveals a continuum of binding modes controlling association and dissociation. *Nucleic Acids Res.* **49**, 11211–11223 (2021).
88. Shi, L. et al. Dissecting the mechanism of atlastin-mediated homotypic membrane fusion at the single-molecule level. *Nat. Commun.* **15**, 2488 (2024).
89. Ha, T. et al. Single-molecule fluorescence spectroscopy of enzyme conformational dynamics and cleavage mechanism. *Proc. Natl Acad. Sci. USA* **96**, 893–898 (1999).
90. Bronson, J. E., Fei, J., Hofman, J. M., Gonzalez, R. L. & Wiggins, C. H. Learning rates and states from biophysical time series: a Bayesian approach to model selection and single-molecule FRET data. *Biophys. J.* **97**, 3196–3205 (2009).
91. Asher, W. B. et al. GPCR-mediated β-arrestin activation deconvoluted with single-molecule precision. *Cell* **185**, 1661–1675 (2022).
92. König, S. L. B. et al. BOBA FRET: bootstrap-based analysis of single-molecule FRET data. *PLoS ONE* **8**, e84157 (2013).
93. Hellenkamp, B. et al. Precision and accuracy of single-molecule FRET measurements—a multi-laboratory benchmark study. *Nat. Methods* **15**, 669–676 (2018).
94. Hilger, D. et al. Structural insights into differences in G protein activation by family A and family B GPCRs. *Science* **369**, eaba3373 (2020).
95. Thomas, T. C., Schmidt, C. J. & Neer, E. J. G-protein alpha o subunit: mutation of conserved cysteines identifies a subunit contact surface and alters GDP affinity. *Proc. Natl Acad. Sci. USA* **90**, 10295–10299 (1993).
96. Deutsch, J. C. Data associated with the publication 'Ligand-dependent G protein dynamics underlying opioid efficacy'. *Zenodo* https://doi.org/10.5281/zenodo.22018761 (2026).

Acknowledgements

We thank E. White for technical laboratory assistance, the L. Lavis lab for the gift of the JFX673-peg4 conjugate fluorophore and R. Sunahara and D. Siepe for helpful discussions.

Author contributions

J.C.D., D.H., J.J., R.V.S., C.M.S., S.C. and B.K.K. designed the single-molecule experiments. J.C.D., J.J. and D.H. purified the proteins. J.C.D. labeled the proteins and prepared the complexes for imaging. J.C.D. performed the GTP hydrolysis and binding assays. J.C.D. and R.V.S. collected and analyzed the single-molecule data. R.V.S., J.C.D. and S.C. developed the imaging platform and code. J.C.D., R.V.S. and B.K.K. wrote the paper and interpreted the results, with input from all authors. R.V.S. and B.K.K. supervised the project.

Funding

Funding support for J.J. was from the National Institutes of Health (NIH; K99GM147609) and the Damon Runyon Cancer Research Foundation (DRG-231 8-18). R.V.S. was supported by an Interdisciplinary Fellowship from the Wu-Tsai Institute (Stanford University). Support for S.C. (R01GM 143554) and B.K.K. (1R35NS137408) was from the NIH.

Competing interests

B.K.K. is a cofounder and consultant for ConfometRx. R.V.S. is a director of clinical pharmacology at Aerys Biosciences. The other authors declare no competing interests.

Additional information

Extended data is available for this paper at https://doi.org/10.1038/s41594-026-01893-6.

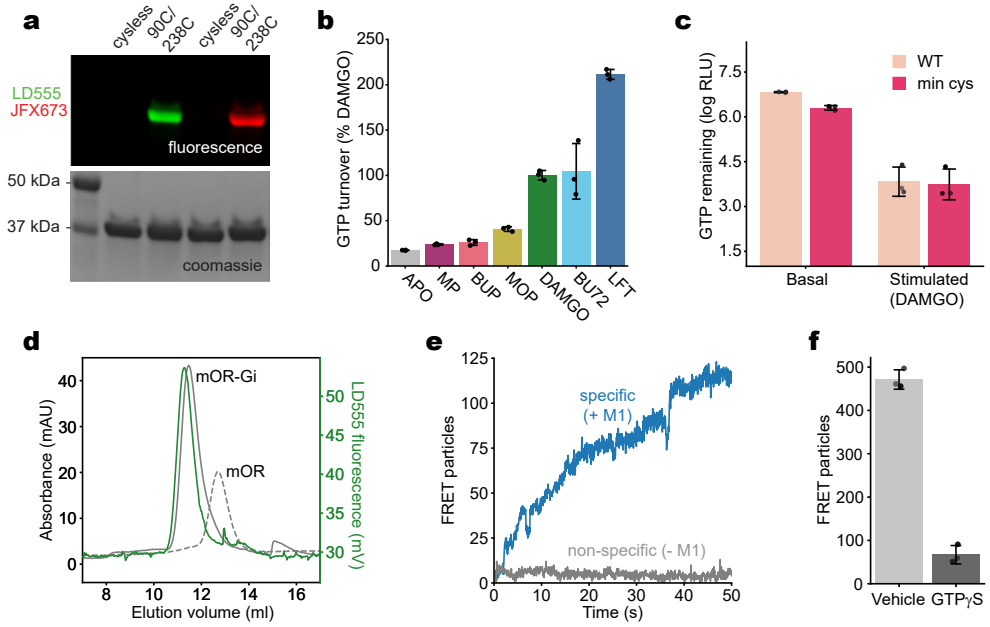
Supplementary information The online version contains supplementary material available at https://doi.org/10.1038/s41594-026-01893-6.

Correspondence and requests for materials should be addressed to Brian K. Kobilka or Rabindra V. Shivnaraine.

Peer review information *Nature Structural & Molecular Biology* thanks Claudiu Gradinaru, Evi Kostenis, Emmanuel Margeat and the other, anonymous, reviewer(s) for their contribution to the peer review of this work. Peer reviewer reports are available. Primary Handling Editor: Katarzyna Ciazynska and Dimitris Typas, in collaboration with the *Nature Structural & Molecular Biology* team.

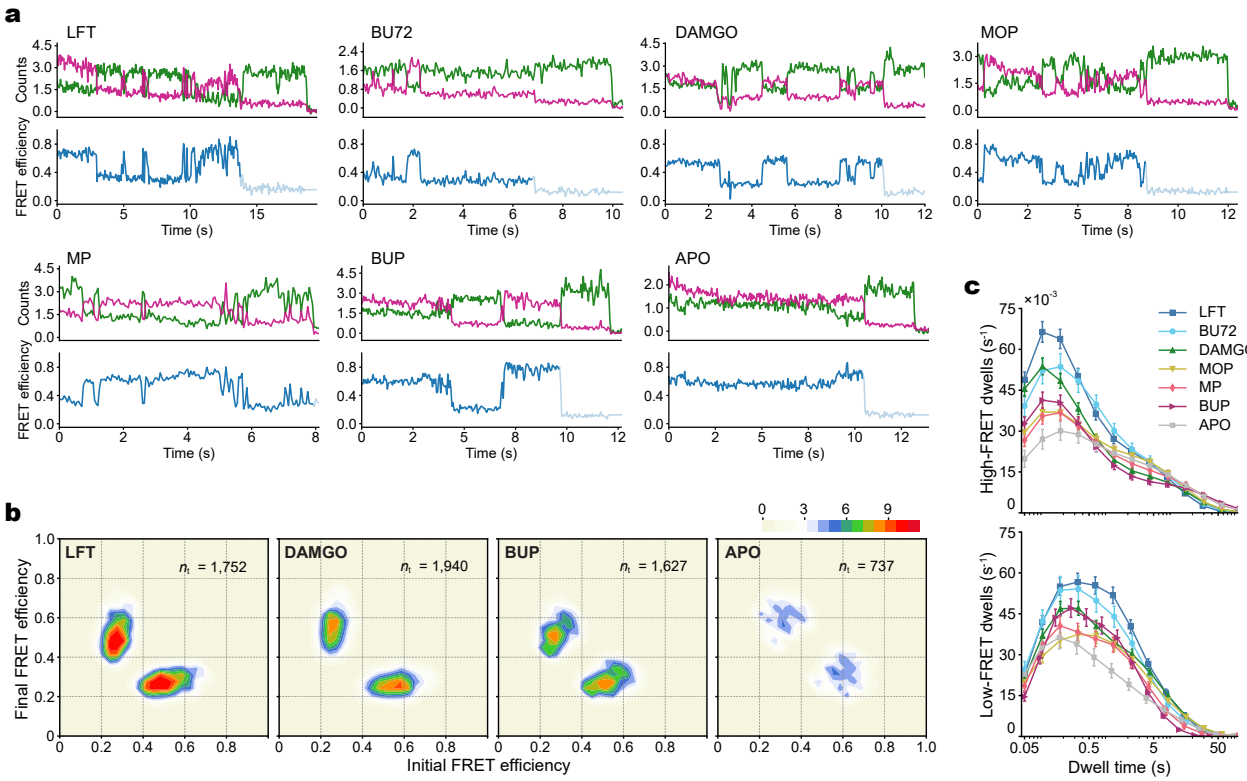
Reprints and permissions information is available at www.nature.com/reprints.

https://doi.org/10.1038/s41594-026-01893-6



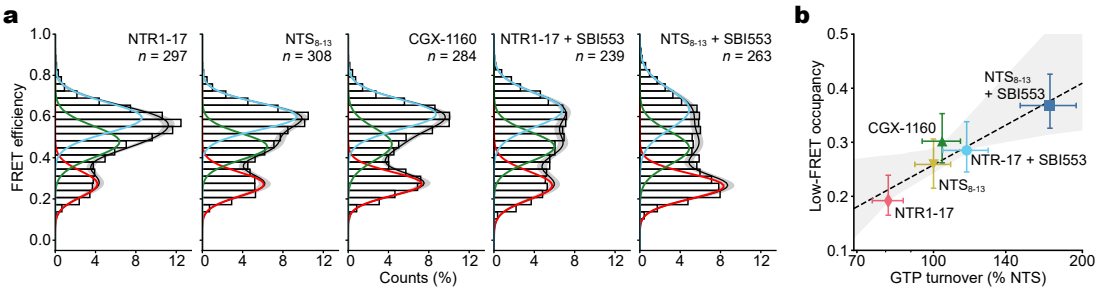
Extended Data Fig. 1 | smFRET experimental controls. a, Site-specific labeling: SDS-PAGE analysis of purified $G\alpha_i\Delta6$ 'cys-less' background with and without engineered cysteines (R90C/E238C) labeled with either LD555 (left) or JFX673 (right) visualized using fluorescence imaging (top; 532 nm or 633 nm illumination), with Coomassie staining (bottom) as a gel-loading control. This experiment was independently repeated twice with similar results. **b**, Ligand efficacy profiles determined from mean WT $G\alpha_i$ GTP turnover assay (Methods). Error bars, s.d. from three technical replicates. **c**, GTP turnover of minimal-cysteine ('min cys') and WT Gαi constructs. Data are mean ± s.d. (n = 3 measurements of the same sample) of the log-transformed RLU (lower signal corresponds to higher activity). **d**, Representative room-temperature size exclusion chromatography (SEC) profiles of buprenorphine-bound μOR alone (dashed line) and as a ternary complex with dye-labeled G_i heterotrimer (absorption in gray; LD555 fluorescence in green). **e**, Specificity of M1 fab-mediated immobilization: Uptake of 200 pM labeled μOR-G_i onto passivated quartz slides coated with M1 fab fragment (blue; specific) and without M1 fab (gray; non-specific) recorded using 100 ms TIRF imaging at low laser power (1 mW at the source) to prevent photobleaching. **f**, Histogram of immobilized FRET particles (mean ± s.d., n = 3 movies of the same sample) remaining after injection of buffer (vehicle) or 10 μM GTPγS into the imaging chamber shows GTPγS binding and functional dissociation of μOR-G_i on the surface.

https://doi.org/10.1038/s41594-026-01893-6



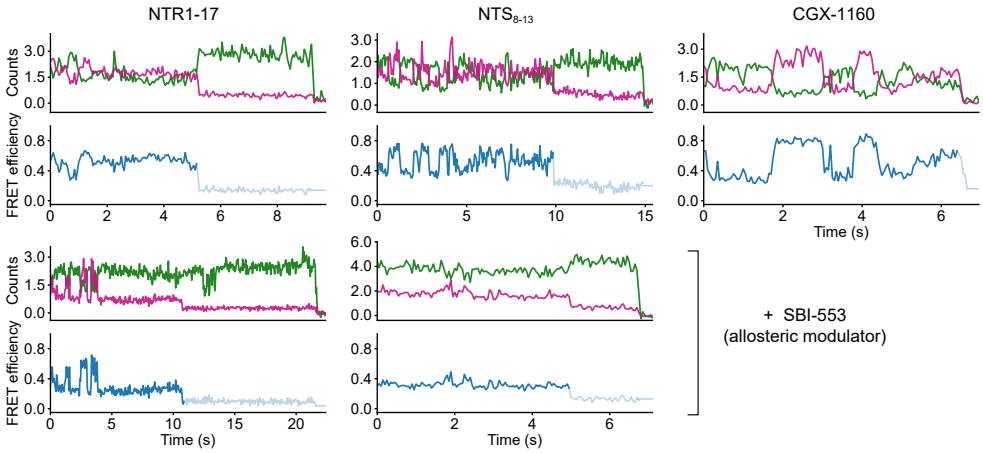
Extended Data Fig. 2 | Analysis of AHD opening and closing in μOR-Gi. **a**, Sample fluorescence (LD555 in green and JFX673 in magenta; units, 10^4 counts) and FRET time traces for M1-Fab-immobilized μOR-G_i complexes in the indicated ligand and unliganded states. **b**, Transition density plots displaying the mean FRET values before (x-axis) and after (y-axis) each transition (n_t total transitions per condition) for a representative selection of the tested ligands. Scale bar, 10^{-3} transitions per bin per second (~ 0.035×0.035 FRET bins). **c**, Dwell time distributions of the μOR-G_i AHD in the open, low-FRET state (top) and closed, high-FRET state (bottom). Error bars, mean ± s.d. of 100 bootstrap samples of the idealized FRET traces.

https://doi.org/10.1038/s41594-026-01893-6



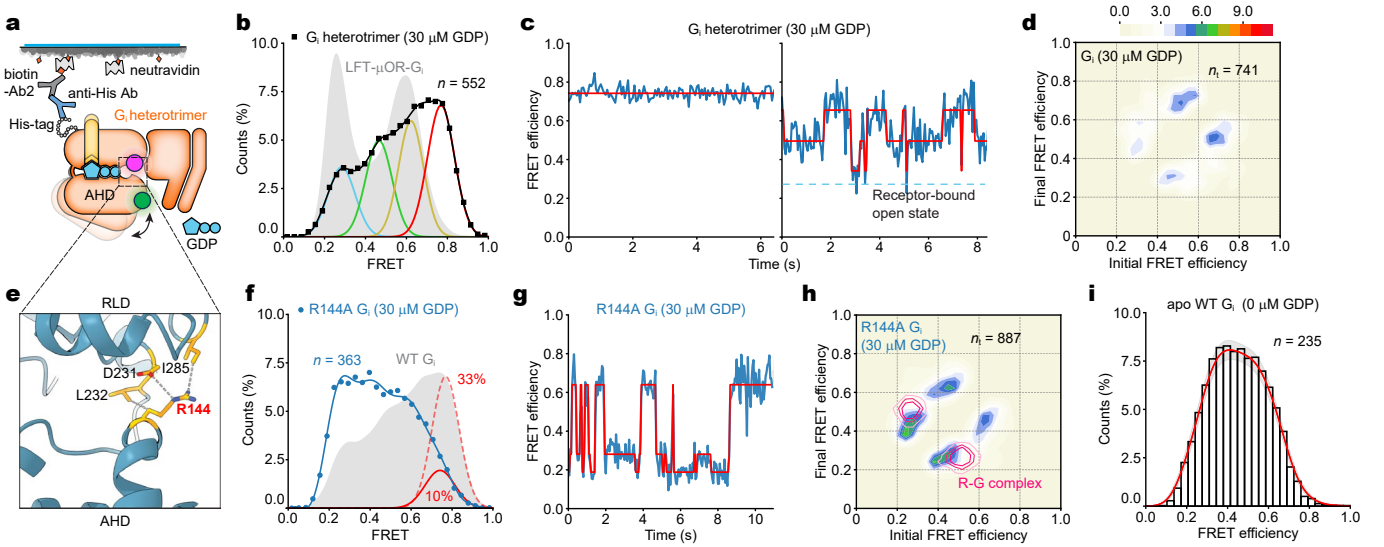
Extended Data Fig. 3 | Ligand-induced AHD separation in NTSR1-G_i. **a**, Apparent population FRET efficiency histograms for NTSR1-G_i ternary complexes bound to the indicated ligands fit to three-state GMMs (black curve), showing the closed (cyan) and open (green and red) states (*n*, number of traces). Error bands, ±1 s.d. of GMM fits from 1000 bootstrap samples of the FRET traces. **b**, Correlation scatter plot of ensemble low-FRET, open-state occupancy (error bars, 95% c.i.) versus log GTP turnover activity (error bars, mean ± s.d. of three technical repeats) with $R^2 = 0.89$. Error band is bootstrapped 95% c.i. of the regression estimate. Ligands include the full agonist NTS_{8-13}, the active fragment of the neurotensin peptide; contulakin-G (CGX-1160), a glycopeptide derivative of NTS found in cone snail toxin; TC-NTR1-17 (NTR1-17), a synthetic partial agonist; SBI-553, an allosteric modulator.

https://doi.org/10.1038/s41594-026-01893-6



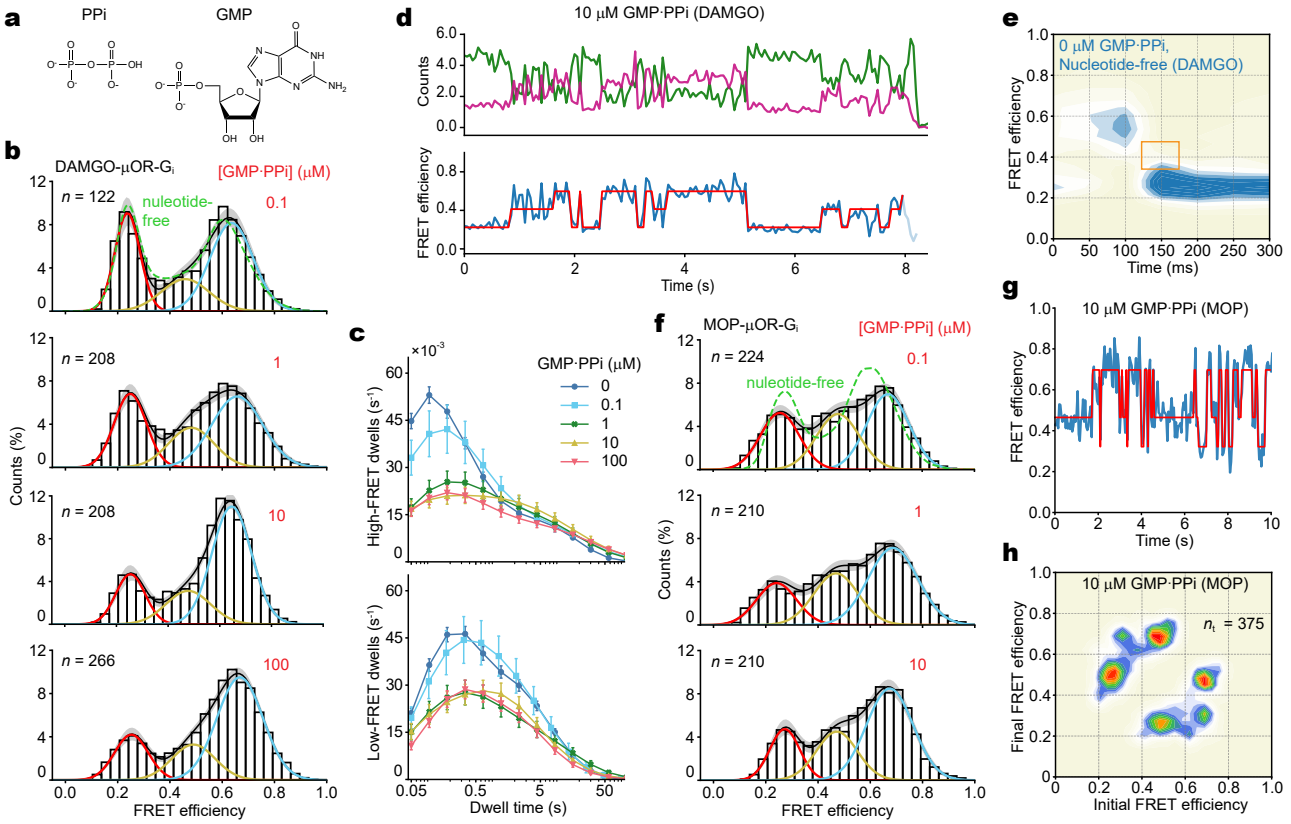
Extended Data Fig. 4 | Example smFRET traces for NTSR1-G_i. Example donor and acceptor fluorescence (LD555 in green; JFX673 in magenta) and FRET traces for surface-tethered NTSR1-G_i bound to the indicated orthosteric and allosteric ligands.

https://doi.org/10.1038/s41594-026-01893-6



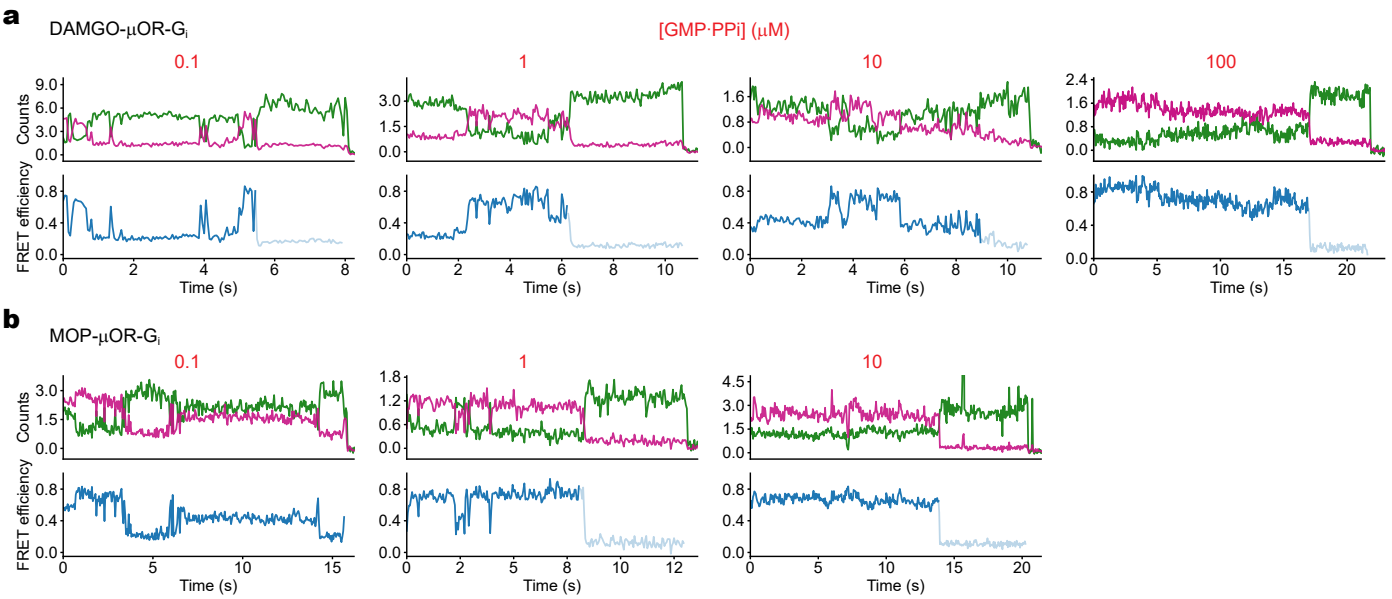
Extended Data Fig. 5 | AHD dynamics in the basal state. a, Labeled $G\alpha_i\Delta 6$-90 C/238 C heterotrimers were tethered to quartz slides via an N-terminal His tag on the Gα subunit and a biotin-mouse antibody bridge. TIRF imaging of the surface-tethered G_i AHD, without and with an alanine substitution at R144, was performed in physiologic 30 μM GDP. **b-d**, Population apparent FRET efficiency histogram (squares; *n*, number of traces) with spline and four-state GMM fits (black and colored lines, respectively) (**b**), example FRET and predicted state traces from two different molecules (**c**), and transition density plot for the parent ('WT') construct in the presence of 30 μM GDP (**d**). **e**, Structure of GDP-bound $G\alpha_{i1}$ (PDB: 1GP2) showing R144 contacts stabilizing the inactive, closed state at the distal interdomain interface. **f**, Population FRET histogram (circles) from imaging R144A shows a low-FRET shift relative to WT (red lines are highest-FRET gaussians with percent occupancy from four-state fits). **g,h**, Example smFRET trace (**g**) and transition density plot (**h**) showing the effects of R144A on AHD dynamics. Pink lines are overlays of major transition density contours generated by a receptor-G protein ('R-G') complex (BU72-μOR-G_i). Scale bar, 10^{-3} transitions per bin per second (cf. Extended Data Fig. 2b). **i**, Apparent FRET efficiency histogram (bars) of surface-tethered Gi in the nucleotide-depleted (apo) state. Shaded error bands, kernel density estimate (red line) ±1 s.d. from 1000 bootstrap resamples of the FRET traces.

https://doi.org/10.1038/s41594-026-01893-6



Extended Data Fig. 6 | Supporting data for μOR-G_i with GMP·PPi. Surface-tethered μOR-G_i was imaged in a buffer containing various concentrations of equimolar GMP and PP_i with either DAMGO- or morphine-occupied receptors. **a**, Structure of PPi and GMP. **b-d**, Population FRET histograms (**b**), dwell time distributions (two-state model; error bars, mean ± s.d. of 100 bootstrap samples of the traces) (**c**), and example dynamic fluorescence and smFRET traces (**d**; 10 μM GMP·PPi) from experiments imaging DAMGO-μOR-G_i. **e**, Synchronization plot of high-to-low transitions in the nucleotide-free state for DAMGO-occupied complex (738 transitions events) (cf. Fig. 3f). **f**, Population FRET histograms from titration experiments with morphine (MOP). **g,h**, smFRET trace (**g**) and transition density plot (**h**) in saturating (10 μM) GMP·PPi from experiments with morphine-bound μOR. Errors bands, ±1 s.d. 1000 bootstrap samples of the traces.

https://doi.org/10.1038/s41594-026-01893-6



Extended Data Fig. 7 | Example smFRET traces with GMP·PPi. a,b, Sample trace recordings of the fluorescence (LD555 in green and JFX673 in magenta; units, 10^4 counts) and apparent FRET efficiency from experiments imaging surface-tethered μOR-G_i bound DAMGO (**a**) and MOP (**b**) in buffer containing the indicated concentrations of equimolar GMP and PPi.

nature portfolio

Corresponding author(s): Brian K. Kobilka
Rabindra V. Shivnaraine

Last updated by author(s): 8/24/2026

Reporting Summary

Nature Portfolio wishes to improve the reproducibility of the work that we publish. This form provides structure for consistency and transparency in reporting. For further information on Nature Portfolio policies, see our Editorial Policies and the Editorial Policy Checklist.

Statistics

For all statistical analyses, confirm that the following items are present in the figure legend, table legend, main text, or Methods section.

n/a	Confirmed
☐	☒ The exact sample size (*n*) for each experimental group/condition, given as a discrete number and unit of measurement
☐	☒ A statement on whether measurements were taken from distinct samples or whether the same sample was measured repeatedly
☐	☒ The statistical test(s) used AND whether they are one- or two-sided *Only common tests should be described solely by name; describe more complex techniques in the Methods section.*
☒	☐ A description of all covariates tested
☐	☒ A description of any assumptions or corrections, such as tests of normality and adjustment for multiple comparisons
☐	☒ A full description of the statistical parameters including central tendency (e.g. means) or other basic estimates (e.g. regression coefficient) AND variation (e.g. standard deviation) or associated estimates of uncertainty (e.g. confidence intervals)
☐	☒ For null hypothesis testing, the test statistic (e.g. *F*, *t*, *r*) with confidence intervals, effect sizes, degrees of freedom and *P* value noted *Give P values as exact values whenever suitable.*
☒	☐ For Bayesian analysis, information on the choice of priors and Markov chain Monte Carlo settings
☒	☐ For hierarchical and complex designs, identification of the appropriate level for tests and full reporting of outcomes
☒	☐ Estimates of effect sizes (e.g. Cohen's *d*, Pearson's *r*), indicating how they were calculated

Our web collection on statistics for biologists contains articles on many of the points above.

Software and code

Policy information about availability of computer code

Data collection	Andor Solis v4.32 (Oxford instruments). Horiba FluorEssence v3.8. MicroBeta2 Windows Workstation v2.1.0.12.
Data analysis	Matlab R2019a/R2023b. smFRET movies were processed using https://github.com/JonathanDeutsch/Freton. vbFRET 2012-12-09,.Python 3.12. sci-kit learn v1.3.2. SciPy 1.11.4. Chimera X 1.6.1. ImageJ Fiji v1.54.

For manuscripts utilizing custom algorithms or software that are central to the research but not yet described in published literature, software must be made available to editors and reviewers. We strongly encourage code deposition in a community repository (e.g. GitHub). See the Nature Portfolio guidelines for submitting code & software for further information.

Data

Policy information about availability of data

All manuscripts must include a data availability statement. This statement should provide the following information, where applicable:

- Accession codes, unique identifiers, or web links for publicly available datasets
- A description of any restrictions on data availability
- For clinical datasets or third party data, please ensure that the statement adheres to our policy

Raw single-molecule traces and idealized trajectories needed to evaluate the conclusions are available through Zenodo at https://doi.org/10.5281/zenodo.22018761 (ref.96). Source data are provided with the paper.

Research involving human participants, their data, or biological material

Policy information about studies with human participants or human data. See also policy information about sex, gender (identity/presentation), and sexual orientation and race, ethnicity and racism.

Reporting on sex and gender	*Use the terms sex (biological attribute) and gender (shaped by social and cultural circumstances) carefully in order to avoid confusing both terms. Indicate if findings apply to only one sex or gender; describe whether sex and gender were considered in study design; whether sex and/or gender was determined based on self-reporting or assigned and methods used.* *Provide in the source data disaggregated sex and gender data, where this information has been collected, and if consent has been obtained for sharing of individual-level data; provide overall numbers in this Reporting Summary. Please state if this information has not been collected.* *Report sex- and gender-based analyses where performed, justify reasons for lack of sex- and gender-based analysis.*
Reporting on race, ethnicity, or other socially relevant groupings	*Please specify the socially constructed or socially relevant categorization variable(s) used in your manuscript and explain why they were used. Please note that such variables should not be used as proxies for other socially constructed/relevant variables (for example, race or ethnicity should not be used as a proxy for socioeconomic status).* *Provide clear definitions of the relevant terms used, how they were provided (by the participants/respondents, the researchers, or third parties), and the method(s) used to classify people into the different categories (e.g. self-report, census or administrative data, social media data, etc.)* *Please provide details about how you controlled for confounding variables in your analyses.*
Population characteristics	*Describe the covariate-relevant population characteristics of the human research participants (e.g. age, genotypic information, past and current diagnosis and treatment categories). If you filled out the behavioural & social sciences study design questions and have nothing to add here, write "See above."*
Recruitment	*Describe how participants were recruited. Outline any potential self-selection bias or other biases that may be present and how these are likely to impact results.*
Ethics oversight	*Identify the organization(s) that approved the study protocol.*

Note that full information on the approval of the study protocol must also be provided in the manuscript.

Field-specific reporting

Please select the one below that is the best fit for your research. If you are not sure, read the appropriate sections before making your selection.

☒ Life sciences ☐ Behavioural & social sciences ☐ Ecological, evolutionary & environmental sciences

For a reference copy of the document with all sections, see nature.com/documents/nr-reporting-summary-flat.pdf

Life sciences study design

All studies must disclose on these points even when the disclosure is negative.

Sample size	No statistical methods were used to predetermine sample sizes, but our sample sizes are similar to those reported in previous publications, eg Zhao et. al, Nature (2024); Latorraca et. al, Nature Chemical Biology (2025).
Data exclusions	No data was excluded from the analysis.
Replication	Attempted replications were successful. G protein activity assays were performed in technical triplicate. smFRET experiments were reproduced in at least two independent attempts. Data from each condition was aggregated with total molecule counts reported.
Randomization	The experiments were not randomized. Covariate adjustment is not applicable to dynamics studies; there is no confounding variables within the datasets that can be statistically controlled.
Blinding	The authors were not blinded during experiments, analysis, or outcome assessments. None of the experiments involved group allocation. Appropriate controls were included during experiments.

Reporting for specific materials, systems and methods

We require information from authors about some types of materials, experimental systems and methods used in many studies. Here, indicate whether each material, system or method listed is relevant to your study. If you are not sure if a list item applies to your research, read the appropriate section before selecting a response.

Materials & experimental systems

n/a	Involved in the study
☐	☒ Antibodies
☐	☒ Eukaryotic cell lines
☒	☐ Palaeontology and archaeology
☒	☐ Animals and other organisms
☒	☐ Clinical data
☒	☐ Dual use research of concern
☒	☐ Plants

Methods

n/a	Involved in the study
☒	☐ ChIP-seq
☒	☐ Flow cytometry
☒	☐ MRI-based neuroimaging

Antibodies

Antibodies used

Biotin anti-mouse IgG1 (BioLegend, cat 406603; 1/25 dilution.
Mouse anti penta·His (Qiagen, cat 34660; 1/50 dilution).
4E11 hybridoma (ATCC, CRL-3623) was not used directly but was processed to generate the M1 (anti-FLAG) Fab.

Validation

Antibodies were validated by their commercial suppliers. Qiagen penta·His was prepared under serum-free conditions.

Eukaryotic cell lines

Policy information about cell lines and Sex and Gender in Research

Cell line source(s)

sf9, Expression Systems, cat 94-001S
Tni (Hi-5), Expression systems, Cat 94011S

Authentication

Cell lines are authenticated by the supplier. No further authenticifcation was performed.

Mycoplasma contamination

Cell lines are tested by the manufacture for contamination, but were not further tested by the authors.

Commonly misidentified lines
(See ICLAC register)

No commonly misidentified lines were used in this study

Plants

Seed stocks

Report on the source of all seed stocks or other plant material used. If applicable, state the seed stock centre and catalogue number. If plant specimens were collected from the field, describe the collection location, date and sampling procedures.

Novel plant genotypes

Describe the methods by which all novel plant genotypes were produced. This includes those generated by transgenic approaches, gene editing, chemical/radiation-based mutagenesis and hybridization. For transgenic lines, describe the transformation method, the number of independent lines analyzed and the generation upon which experiments were performed. For gene-edited lines, describe the editor used, the endogenous sequence targeted for editing, the targeting guide RNA sequence (if applicable) and how the editor was applied.

Authentication

Describe any authentication procedures for each seed stock used or novel genotype generated. Describe any experiments used to assess the effect of a mutation and, where applicable, how potential secondary effects (e.g. second site T-DNA insertions, mosiacism, off-target gene editing) were examined.